Plasmonics
https://doi.org/10.1007/s11468-026-03476-z

RESEARCH

Metal-Filled Porous Silicon for Plasmonic Light Trapping in Solar Cell Applications: A Comparative Finite Element Study of Ag, Au, and Cu

Muhammad Naseem Akhtar[1] · Tahir Iqbal[2] · Hamaad Ali[2] · Muhammad Azhar Naeem Gilani[3] · Muhammad Riasat[2] · Roha Jehangir[2] · Guido Mula[1]

Received: 24 July 2026 / Accepted: 15 September 2026
© The Author(s) 2026

Abstract

Crystalline silicon (c-Si) solar cells currently dominate with commercial module efficiencies of 22–24% and laboratory records ~ 27% for single junction devices. These values are constrained by optical losses, including insufficient light trapping within the device architecture. In this study we report a finite element analysis (FEA), carried out in COMSOL Multiphysics RF Module (v.5.3a), of a one-dimensional porous silicon array (1D PSiA) with pores filled by silver (Ag), gold (Au), and copper (Cu) in a c-Si substrate, targeting enhanced light trapping through surface plasmon polaritons (SPPs) and localized surface plasmon resonance (LSPR). Pore width (w) was swept from 50 to 600 nm at a fixed periodicity (Λ) of 700 nm under transverse-magnetic (TM) illumination. Far-field transmission spectra reveal a Fano-resonance dip at 703–720 nm governed by the structural periodicity. Full-width at half-maximum (FWHM) and near-field electric-field norm (E-Norm) analysis identify $w = 200$ nm as the critical coupling width for Ag (E-Norm peak 0.0044 a.u.) and $w = 200$–250 nm for Au and Cu (0.0045 and 0.0040 a.u.). Coupling efficiencies (η) at $w = 200$ nm reach 97.2%, 96.4%, and 95.4% for Ag, Au, and Cu, respectively, saturating above 99% for $w \geq 250$ nm; relative transmission (T_{rel}) peaks near 0.029 a.u. at $w = 250$ nm before declining sharply. A four-way correlation of FWHM, E-Norm, η, and T_{rel} is consistent with the optimum pore widths correspond to roughly one-third of the structural periodicity, offering a computationally validated geometric design rule for pore-confined plasmonic solar cell fabrication.

✉ Muhammad Naseem Akhtar
mnaseemakhtar@dsf.unica.it

✉ Tahir Iqbal
tahir.awan@uog.edu.pk

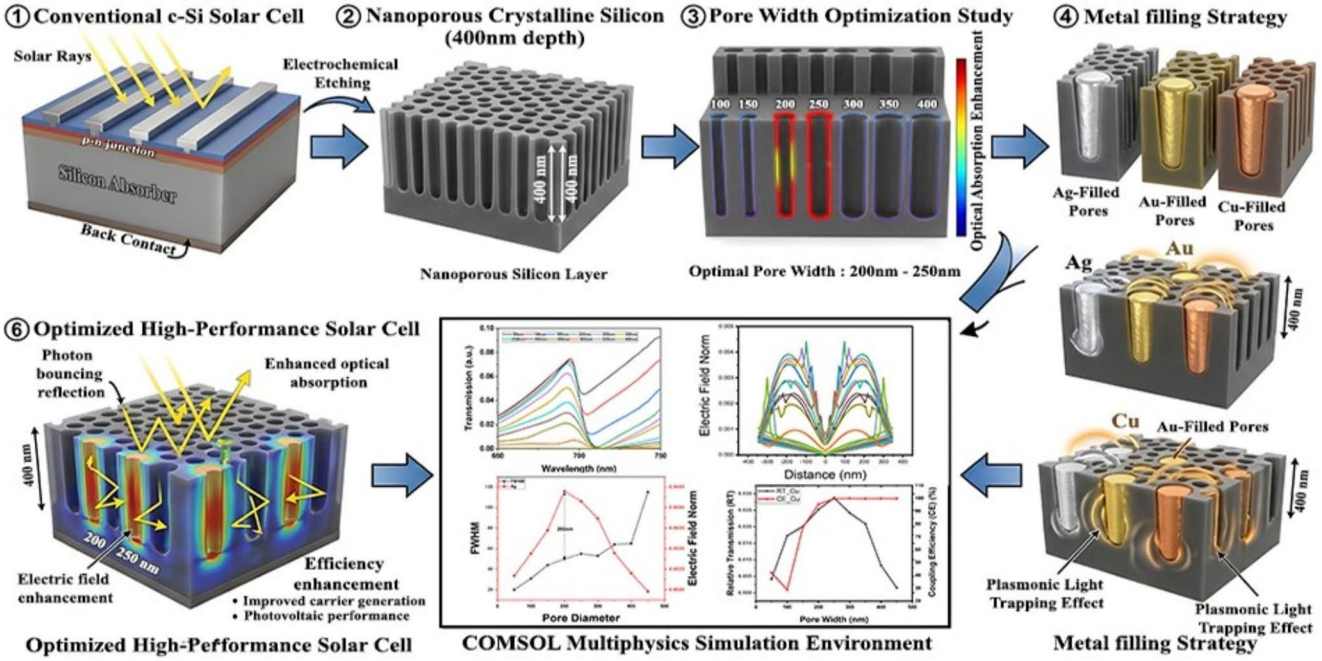
[1] PoroSiLab, Dipartimento di Fisica, Università degli Studi di Cagliari, Cittadella Universitaria di Monserrato, S.P. 8 km 0.700, Monserrato (Ca), Italy

[2] Department of physics, Faculty of Science, University of Gujrat, Hafiz Hayat Campus, Gujrat 50700, Pakistan

[3] Department of Physics, Faculty of science, University of Sialkot, Sialkot 51310, Pakistan

Published online: 24 September 2026

Graphical Abstract



Keywords Porous silicon array · Plasmonic solar cell · Finite element analysis · Surface plasmon polariton · Fano resonance

Introduction

Clean and renewable energy represents a pressing global need. Research activity in this field has intensified significantly, driven by efforts to advance solar cell technologies. There are lots of options available but still crystalline silicon (c-Si) solar cells are dominating the photovoltaic market with commercial module efficiencies of 22–24% and laboratory records ~ 27% for single junction devices [1, 2]. These values are constrained by optical losses, including insufficient light trapping within the device architecture. These cells come with a thick active layer of 130–180 µm that not only increases material consumption but also the production cost [3–5]. Thin film solar cells have the potential to address these issues but they also have their own challenges like, shorter absorption length and high bulk recombination. These are the reasons why researchers these days are looking for the hybrid engineered materials like nanostructured light trapping architectures. In this category, plasmonic metallic gratings and porous semiconductors have emerged as promising architectural candidates [3, 5–7]. Plasmonic nanostructures provide an effective approach for manipulating light at the subwavelength scale through the excitation of surface plasmon polaritons and localized plasmonic modes. The strong electromagnetic-field confinement associated with these modes can enhance light–matter interactions and improve optical absorption in nanoscale structures. In particular, metallic nanostructures integrated with silicon have attracted considerable interest because they can facilitate efficient coupling of incident light into confined optical modes and extend light interaction beyond the conventional absorption limits of thin silicon layers [8].

In order to develop these architectures, it is necessary to excite surface plasmon polaritons (SPPs). SPPs are the collective oscillations of free electrons at the metal-dielectric interface, arising when there is a resonance match between the momentum of incident photons and the wave vector of the electron plasma wave propagating along the metal surface [9–12]. These SPPs provide an efficient mechanism for concentrating optical energy within thin active layer: the electromagnetic field is dramatically enhanced near the metal surface. Momentum matching for SPP excitation cannot be satisfied by a planar metal film under direct illumination; therefore, periodic grating structures supply the necessary reciprocal-lattice momentum via Bragg diffraction [13–15]. The coupling efficiency (η) and the nature of the dominant plasmonic mode are determined by the slit width (w), film thickness, and periodicity (Λ) of the grating [12]. A study reports a maximum η of 88.5% in a one dimensional (1D) sinusoidal gold (Au) grating on c-Si, simulated using the finite elemental analysis (FEA) in COMSOL Multiphysics RF Module at a slit width equal to half of the periodicity (w

= Λ/2 = 350 nm at Λ = 700 nm), considering the fact that sinusoidal geometry favors only the fundamental harmonic, and therefore produces no higher-order modes that would scatter SPPs and reduce η [16]. A study on amorphous silicon (a-Si) with rectangular gratings of Au and silver (Ag) optimized the slit width and slit thickness for a Λ of 720 nm, finding the optimal slit width to be one-third of the Λ (w ≈ 240 nm), which showed consistent minimum Full-width at half-maximum (FWHM) for the resonance dip with maximum constructive interference of co-propagating SPP modes [17]. Both studies employed near-field and far-field analysis, and their correlation, to confirm SPP excitation.

A broad variety of grating profiles have been studied for solar cell absorption enhancement. Trapezoidal gratings on c-Si improved optical efficiency by up to 32% relative to flat-cell references [18], while diffractive Si rear gratings boosted short-circuit current density by 76.5% in thin-film polycrystalline silicon cells. Pyramid and nanosphere front-surface gratings have achieved power conversion efficiency (PCE) values of up to 26.06% in perovskite architectures, and double-grating designs produced 65% light absorption in organic active layers [19–21]. Triangular gratings generate sharper resonance peaks than several other profiles [17], whereas sinusoidal gratings suppress higher-order plasmonic harmonics, yielding the most efficient fundamental-mode coupling [16, 22]. Au is selected for its near-infrared plasmonic response and chemical stability; Ag is chosen for its lower optical losses in the visible spectral region. Copper (Cu) is an economically attractive plasmonic material having plasmonic response similar to Au and it is particularly less studied in pore-confined configurations, this is a motivation behind the inclusion of Cu in this study. As the grating slit width approaches its optimal value, the FWHM of the SPP resonance dip decreases, thereby increasing the coupling efficiency, this is a design rule that links geometrical parameters to device performance [16, 17]. When we integrate the metals like Ag, Au and Cu into the porous silicon (PSi), enhanced optical light trapping employing the localized surface plasmon resonance (LSPR), which is a localized field enhancement caused by oscillating electrons that creates highly amplified electromagnetic fields at the nanoparticle surfaces and remain localized at sharp tips or within nanoscale dimensions (hotspot) like edges of the metal [23]. Ag and Au offer superior field enhancement, complementing or replacing them with earth-abundant Cu presents a highly cost-effective path toward commercial scalability, optimizing light-trapping and carrier collection via gradient refractive-index (n) matching within the 1D porous architecture [24, 25] PSi, with its high surface-to-volume ratio, tunable n, and intrinsic broadband antireflection character arising from its graded *n* profile, can serve as a versatile host for plasmonic metals in enhanced optical light trapping [26, 27].

Fano-resonance line-shapes analogous to those reported here have also been exploited in plasmonic sensing architectures, for example the multichannel refractive index and temperature sensor of Chou Chao and Chou Chau [28], which underscores that the asymmetric Fano line-shape is a general signature of grating coupled plasmonic structures rather than a feature unique to the present geometry. The periodic metal-shell rod array of Chao et al. [29] a narrowband plasmonic absorber whose resonances are set by geometry rather than by composition and which is analyzed with the same finite element approach adopted here, offers a further point of comparison for the subwavelength metal-filled pore walls of the present structure, whose optical response is governed by pore shape and not by porosity alone [26].

Infiltrating noble or transition metals (Ag, Au, or Cu) into the pore network creates hybrid nanocomposites that combine effective antireflection with plasmonic light concentration [30]. For instance, hybrid PSi/Ag structures have shown near-unity broadband optical absorption [23, 25]. Furthermore, incorporating these configurations into metal-insulator-semiconductor (MIS) solar cells has substantially increased short-circuit current density, open-circuit voltage, and overall PCE [31–33]. In this study, a c-Si substrate with periodic rectangular pores infiltrated with plasmonic metals (Ag, Au, and Cu) was modelled and systematically investigated. This architecture, referred to hereafter as a one-dimensional porous silicon array (1D PSiA), was selected because its periodic geometry provides the reciprocal lattice momentum necessary for efficient SPP excitation under transverse magnetic (TM) illumination. Most prior simulations address single-metal planar grating geometries, 3D Finite-Difference Time-Domain (FDTD) analyses of isolated nanoparticles in perovskite or organic devices or surface-deposited rather than pore-confined metal fills [34, 35].

The studies cited above leave specific gaps that the present work addresses. First, Saeed et al. [16] and Iqbal et al. [17], and Ahsan et al. [36] which are the most closely related FEA studies, use sinusoidal and surface-deposited rectangular, and MoS_2-Ag rectangular/triangular gratings, respectively, and Chou Chau et al. [29] use a square-lattice array of silver-shell dielectric-core nano-beads deposited onto a crystalline silicon layer, whereas the present work considers metal fills confined within the pores of a c-Si host. This pore-confined geometry is physically distinct in which the metal is enclosed on all sides by the semiconductor, which alters the modal structure, supports stronger LSPR at pore corners, and changes the effective dielectric environment relative to a surface-deposited metal layer. Second, Iqbal et al. [17] use a-Si as the substrate; the present work uses c-Si, which has a markedly different permittivity dispersion (Palik [37]) and is the industry-standard photovoltaic

material. Third, Cu is despite being an economically attractive plasmonic metal for large-scale fabrication has not been included in any prior pore-confined 1D FEA study of this type. Fourth, most prior simulations treat only a single metal while the present side-by-side comparison of Ag, Au, and Cu under identical simulation conditions provides a directly comparable, geometry-resolved dataset that can guide material selection for MIS plasmonic solar cell fabrication.

A unit cell of 1D PSiA with Ag, Au and Cu metal fillings which is used for this investigation is mentioned in Fig. 1(a) and Fig. 1(b) describes a periodic structure simulated with different boundary constraints and subdomains describing PSi host and metal fillings. Present study addresses this gap by using FEA modelling in the COMSOL Multiphysics RF Module (v. 5.3a) to simulate a 1D array of rectangular, metal-filled pores in c-Si substrate with a fixed Λ of 700 nm.

The objectives of the present work are: (i) to conduct the far field and near field analysis of Ag, Au & Cu filled 1D PSiA, (ii) to study the η and T_{rel} of this array, (iii) to identify the optimized *w* for enhanced light trapping for all the three metals used hence providing a reliable simulation-backed design for actual fabrication of metal filled PSi plasmonic solar cell.

Theoretical Modelling Framework

When we excite the surface plasmons (SPs), the electromagnetic field attains its highest value at the metal-air/Si boundaries hence creating LSPR, confined within the pore geometry and SPPs, propagating along the metal wall owing to the analogy between 1D PSiA and rectangular grating [23, 38]. The formation of SPPs requires a strict momentum matching this implies that the resonance is dependent of the incident angle and wavelength of the light [39–41]. Considering the morphology of the PSiA, grating coupling approach is employed that provides the necessary momentum matching required for the excitation of SPPs. It should be noted that real pore geometry is often random and irregular but utilizing PSiA provides us clean, predictable optical trends.

When the incident light strikes this periodic array, it generates a series of diffracted orders. Instead of scattering away into free space, these specific modes remain bound tightly to the boundary due to the exponential decay of their electromagnetic fields, functioning as evanescent modes [12, 42]. Crucially, this periodic setup does dual work: while the overall grating profile bridges the momentum gap for propagating SPPs along the top surfaces, the subwavelength metal walls of the rectangular pores independently trap light to trigger LSPR [23, 43].

The 1D porous grating design is well correlated with the wavelength (λ_o) of incidence electromagnetic waves. To trigger SPPs, the incoming light must receive a momentum increment Δkx along the the interface to bridge the gap between surface plasmon (SP) wavevector and incident light wave vector [43]. The grating diffraction condition governs this 1D coupling mechanism as:

$$\sin\ \theta_N = \sin\ \theta_i + \frac{N\lambda\,o}{\Lambda} \tag{1}$$

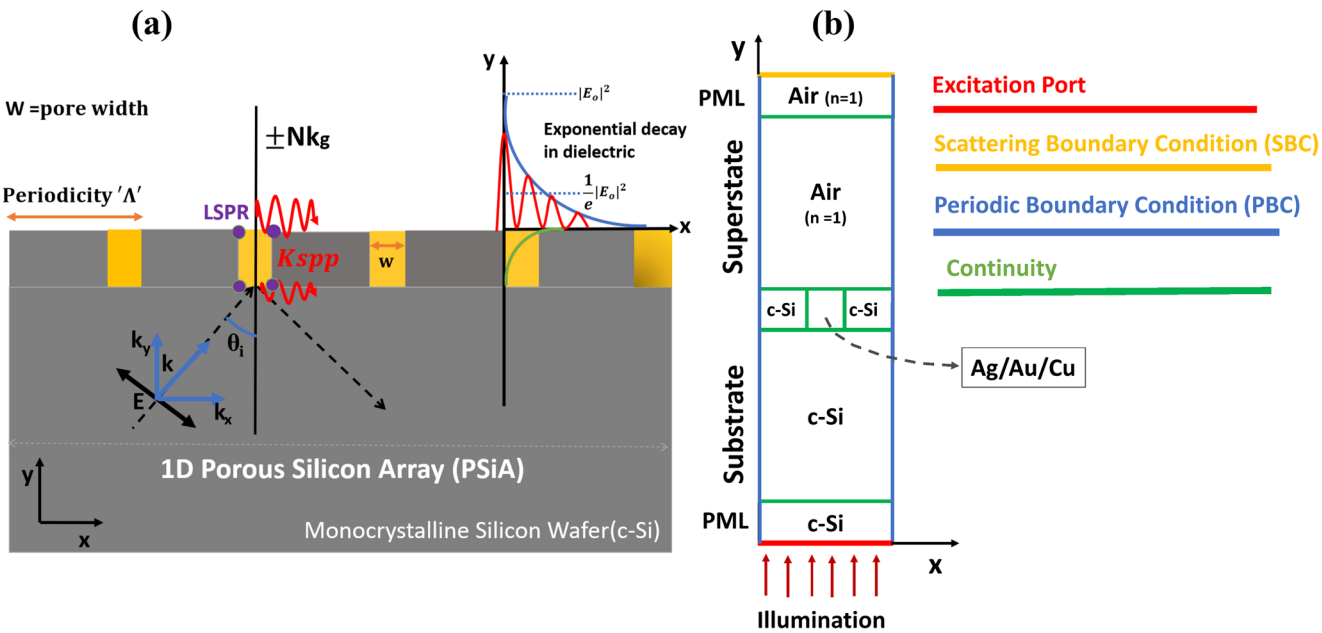


Fig. 1 (**a**) Schematic of 1D PSiA showing SPPs and LSPR excited at interfaces by coupling of incoming photons with metal SPs, (**b**) a simulated unit cell in the COMSOL Multiphysics with boundary conditions and different subdomains

Where θ_N is the angle of N-th diffracted order and θ_i is the angles of incidence, n is order of diffraction (N = ± 1, ± 2,….), and Λ is the structural periodicity of our unit cell (700 nm) [44]. To derive an equation for the momentum matching condition for exciting SPPs, we multiply both sides of Eq. (1) by free-space wave vector $k_\circ = \frac{2\pi}{\lambda_\circ}$ and we get:

$$k_{spp} = k_\circ sin\ \theta_i \pm n\ k_g \quad (2)$$

where, *kspp* is the SPPs wave vector at the metal-air/Si interface, and $k_g = \frac{2\pi}{\Lambda}$ represents reciprocal lattice vector provided by the lattice geometry. This resonance condition can only be satisfied by p-polarized light which is transvers magnetic (TM), because in this light the electric field oscillates perpendicular to the metal walls that conveniently make the surface charge to oscillate needed to excite SPPs. Whereas in s-polarized light which is transverse electric (TE), the electric field oscillate parallel to the metal wall hence not able to make the surface charge oscillate, therefore, no SPPs excitation for TE light. Therefore, this relationship serves as our foundation framework for mapping how plasmonic resonance wavelength (RW) varies across Ag, Au, and Cu configurations by changing the geometry and incident angle [14, 39, 45, 46].

Geometry Construction and Numerical Modeling

The geometry of the model was constructed using built-in Computer-Aided Design (CAD) tools present within COMSOL Multiphysics (v. 5.3a) which solves the Maxwell's equations across the computational domain governing the model. The computational domain is divided into subdomains, each of these is assigned a material parameter and a wavelength-dependent complex permittivity function. The required optical constants and refractive index data were assigned via the built-in materials library.

The schematic layout and the corresponding 1D plasmonic crystal array are illustrated in Fig. 1(a, b). The Fig. 1(a) illustrates the excitation and confinement of plasmonic modes within a metal filled 1D PSiA. **E** is the polarization direction, k_x and k_y are the components of momentum vector formed by the TM light incident at θ_i. This light receives a momentum increment of $\pm Nk_g$ from the structural periodicity, to satisfying momentum matching condition that enables photon coupling into the propagating SPPs (K_{spp}) along the interface LSPR is excited at the sharp edges of the metal-filled pores due to charge accumulation and the resulting electromagnetic field is highly modulated along x-axis due to periodic slits. The optical energy is tightly bounded to the metal-dielectric interface because the field ($|E_0|^2$) exhibit evanescent behavior showing an exponential decay ($\frac{1}{e}$) of its intensity peek at sub-wavelength distance. To model an infinitely repeating 1D array while optimizing computational resources, appropriate boundary conditions were enforced. Floquet periodic boundary conditions (PBCs) (blue) were applied to the lateral boundaries of the unit cell [47]. Plane-wave illumination was introduced from the lower boundary via an optical Port (red). To prevent unphysical back-reflections and simulate an open boundary environment, a Scattering Boundary Condition (SBC) (yellow) was implemented at the upper boundary of the superstrate. Additionally, a Perfectly Matched Layer (PML) was positioned beneath the c-Si substrate and above superstrate (air) region to efficiently absorb highly confined, non-radiative evanescent waves [48], and accommodate large wave vectors along the lower calculation boundary thereby extending the computational domain to λ/2 [12, 16]. Hence, PMLs ensure the directional flow by absorbing waves travelling through certain wave directions by coordinate transformation [17, 49]. All the internal boundaries of sub-domains are assigned with continuity boundary condition (green). In the Fig. 1(b) the different boundary conditions employed at the unit-cell boundaries and various subdomains used are shown, each of these represents the different materials used in the simulation.

The coarse mesh size was 20 nm and the minimum mesh element size was kept at 5 nm near the interface. FEA was implemented via the RF Module of COMSOL Multiphysics (v. 5.3a) to simulate the optical response of the system. The Λ was maintained at a constant 700 nm to provide the necessary phase matching and the simulation subdomains are assigned with optical functions and *n* of c-Si, Ag/Au/Cu and air as per the requirement.

To confirm that the reported results are independent of spatial discretization, a mesh convergence study was performed for the Au-filled PSiA at the critical w=200 nm. Keeping the other parameters constant, eleven mesh configurations were evaluated, spanning the pre-defined COMSOL mesh sizes (coarse through extremely fine) and five custom element sizes (20, 15, 10, 5, and 2.5 nm), as summarized in Table 1. The resonance wavelength was recorded for each configuration as the convergence metric. The pre-defined mesh sizes (coarse through finer) produce resonance wavelengths ranging from 801 nm down to 715 nm, reflecting strong sensitivity to spatial discretization at these element sizes, where the mesh is too coarse to resolve the intense near-field gradients at the metal-dielectric interfaces. Convergence is achieved at the Custom 20 nm level: the RW stabilizes at 716 nm and deviates by no more than 1 nm across all finer configurations (Custom 15 nm, 10 nm, 5 nm, and 2.5 nm), satisfying the adopted convergence criterion of a shift below 1 nm between successive mesh refinement levels. The Custom 20 nm mesh (26,276 elements; 106,286 degrees of freedom) was therefore

Table 1 Mesh convergence study for the Au-filled 1D PSiA at w=200 nm showing resonance (RW) stability across eleven successive mesh configurations

Sr no.	Mesh Size	No. of Elements	Degrees of Freedom	Solution Time (s)	RW (nm)
1	Coarse	150	682	54.282	801
2	Normal	188	846	57.444	772
3	Fine	216	966	58.248	768
4	Finer	374	1038	70.418	715
5	Extra Fine	980	4158	125.472	714
6	Extremely Fine	3576	14,770	401.854	716
7	Custom (20 nm)	26,276	106,286	2824.747	716
8	Custom (15 nm)	36,434	147,322	3428.082	716
9	Custom (10 nm)	39,132	158,890	3717.828	716
10	Custom (5 nm)	61,428	250,434	4301.312	716
11	Custom (2.5 nm)	111,366	454,906	8424.268	716

retained for all subsequent simulations, as it provides an optimal balance between numerical accuracy and computational efficiency, with a solution time of approximately 47 min compared to over 140 min for the Custom 2.5 nm configuration.

This study employs a computational approach; minor quantitative deviations from experimental results are therefore expected. Nevertheless, the physical mechanisms demonstrated here provide rigorous motivation for the fabrication of the proposed plasmonic solar cell.

The complex relative permittivity of the constituents is mathematically expressed through its real and imaginary parts as $?_r = ?' + i?''$, where the real component ($?'$) shows the phase response and spatial scattering profile, while the imaginary component ($?''$) represents the ohmic absorption and thermal dissipative losses. These components are related to the n and extinction coefficient (k) via $?' = n^2 - k^2$ and, $?'' = 2nk$ respectively [17, 50].

In this work, the wavelength-dependent complex optical constants for the noble metal fills Ag, Au, and Cu were obtained from the foundational experimental frameworks established by Johnson and Christy [51, 52]. For the host semiconductor matrix, the dielectric functions of c-Si were extracted from the standard compilations by Palik [37], and their plots are shown in the Fig. 2(a-d). These optical parameters were integrated into the simulation materials library and dynamically interpolated using the built-in solver of COMSOL (v.5.3a), to precisely evaluate the spatial electric field distributions within each computational sub-domain.

The selected noble metals (Ag, Au, Cu) exhibit high free-electron densities and low optical dampening profiles within the ultraviolet to near-infrared (UV-Vis-NIR) spectral regimes [53]. At optical frequencies, these metals exhibit a large negative real permittivity ($\epsilon'_m < 0$). To sustain a bound, non-radiative SPP mode along the flat horizontal

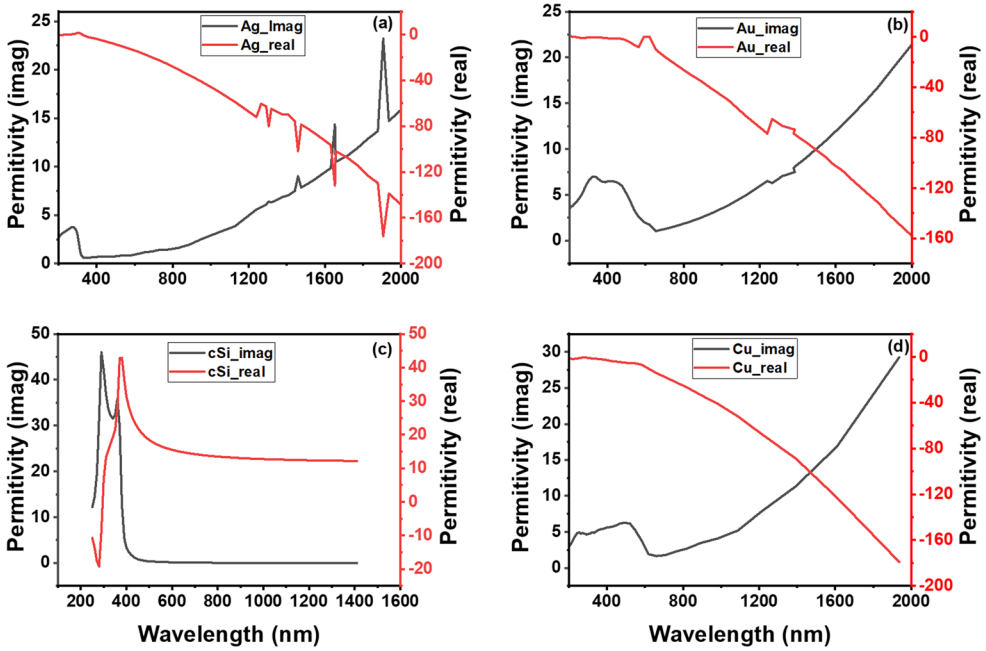


Fig. 2 The plots of real and imaginary parts of permittivity values for (**a**) Ag, (**b**) Au, (c)c-Si and (**d**) Cu

boundaries of the array, the real parts of the permittivities at the heterogeneous interface must possess opposite signs and satisfy the foundational condition:

$$\mathrm{Re}\,(\epsilon_m + \epsilon_d) < 0 \tag{3}$$

Here, ϵ_m and ϵ_d shows the complex permittivities of the metal fill and the adjacent dielectric medium (c-Si or air) [17, 54, 55]. In this way the electromagnetic field remains tightly localized at the boundaries, depicting a sharp exponential attenuation normal to the interface [56, 57].

The wave-matter interactions inside the 1D PSiA are simulated in the frequency domain. First, Maxwell's curl equations are applied under periodic boundaries and port illumination. Next, an adaptively refined, unstructured finite element mesh splits the domain into small pieces to resolve the intense near-field gradients at material borders from where electric field is computed which is post processed for the field enhancement spectra, reflectance and transmittance. COMSOL Multiphysics is a well-established, versatile finite element platform capable of simulating complex electromagnetic problems with rigorous accuracy [58, 59].

There is another advantage here which is in the form of employing the FEA. It is preferred over tools such as FDTD, because, it breaks the simulation area down into an unstructured mesh of small, connected pieces called mesh elements [60]. Whereas, FDTD uses a rigid, rectangular grid that creates jagged "staircasing" errors on sharp edges [61].

In this way we can pack the interface edges with a large number of mesh elements that can capture captures intense, localized plasmonic hotspots i.e. LSPR without expending computational resources on regions of low field gradient.

Baseline Normalization and Model Validation

Before initiating the parametric simulations, a strict normalization and calibration procedure was performed to establish a reliable simulation baseline. At first, the n of all subdomains was set to unity ($n = 1$), creating a homogeneous vacuum environment after that the port was excited with TM-polarized light, which produced an exponential transmission curve, as shown in Fig. 3(a). The text file of this curve was then exported and reintroduced into the global definitions as a calibration interpolation function in order to remove system-induced propagation effects. We then ran the simulation again that leads to the normalized transmission spectrum which is a constant, wavelength-independent horizontal line at unity (Transmission = 1), as shown in Fig. 3(b). Now we compared the spectral data for Reflection (R), Transmission (T), and Absorption (A) with analytical results derived from the Fresnel equations. For structural validity and numerical accuracy of the model the conservation of energy must be satisfied, i.e., R + T + A = 1. This confirms that all incident light is correctly accounted for as transmitted, reflected, or absorbed energy. The model is then operated under both p-polarized i.e. TM and s-polarized i.e. TE modes. These Electromagnetic (EM) fields are resolved into their respective components i.e. E_x, E_z, H_z for the TM and E_y, H_x, H_z for the TE modes. The close matching between these analytical Fresnel calculations and the steady-state computational results confirms the rigorous validation and mathematical reliability of the simulation framework [12, 14, 17, 55].

As an additional quantitative benchmark, the present COMSOL model was applied to a geometry closely matching that reported by Iqbal et al. [17]: a 240 nm Au grating with 50 nm film thickness on a 720 nm unit cell, using identical materials, boundary conditions, and optical constants. This reproduction gave a resonance wavelength of 747 nm and a coupling efficiency of 93.331%, closely matching the reference values of 745 nm and 83%. We then introduced pore confinement into this same validated model, changing only the geometry: a metal-filled pore of 400 nm depth and 40 nm width, with all other parameters held fixed. This single change shifted the resonance to 737 nm and raised the coupling efficiency to 99.93%. Because every other parameter was held constant between the two simulations, this comparison isolates the observed improvement specifically to pore confinement.

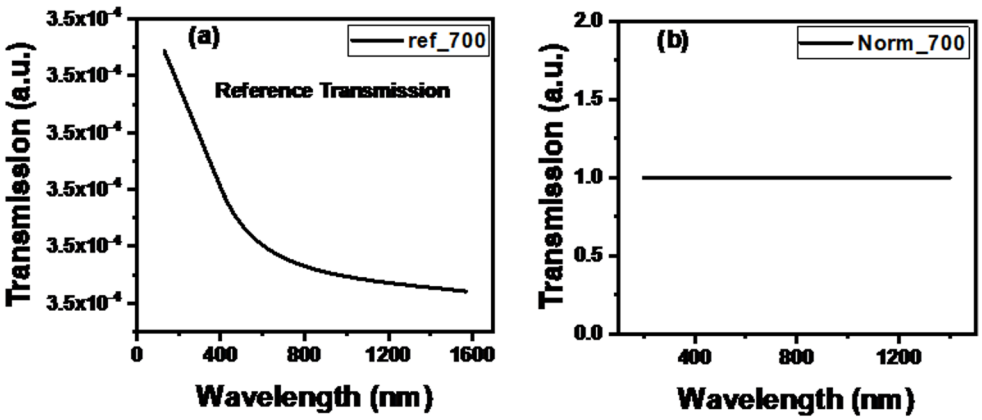


Fig. 3 **(a)** Transmission spectra when all subdomains have n equal to unity **(b)** Transmission spectra after introducing the reference data set as interpolation function

The objective of our research work is the optimization of monocrystalline PSi wafer filled with metals (Au, Ag, Cu) for developing plasmonic based solar cells. The optimization is carried out by varying the pore diameter and metal type inside the pores like Au, Ag and Cu and then performing near field and far field analysis and calculating their T_{rel} and η.

Results and Discussion

Optimization of Pore Width

The optimization of *w* is carried out by performing far-field and near-field analysis of metal-silicon and metal-air interfaces by observing the dips corresponding to SPP excitation in their transmission curves and their field enhancement along the interfaces. The transmission spectrum is obtained by illuminating the port of the model with TM light. Since the E-field components are perpendicular and parallel to the direction of propagation, TM light excites SPPs on the metal (Au, Ag, Cu)-silicon and metal-air interfaces, corresponding to the resonance dips in the transmission curves. TE light, on the other hand, does not excite SPPs, as its electric field is parallel to the surface [16, 62, 63]. The details of the geometrical parameters used in the simulation are listed in the Table 2.

Far-Field Transmission and Fano Resonance

It is the analysis of transmitted electromagnetic waves at a distance significantly greater than the operating wavelength ($r >> \lambda$), where 'r' is distance from the plasmonic interface, where the localized near-field chaos produced by non-propagating evanescent modes decays completely, yielding stable, outward-propagating wavefronts. The far-field transmission spectra of the periodic 1D PSiA inside a thick c-Si substrate is displayed in Fig. 4(a-f), the Figure shows the transmission spectrum of Ag, Au and Cu for *w* ranging from 50 nm to 600 nm. The spectrum is a sharp asymmetric profile instead of normal symmetric peaks, the curves show a maximum transmission at $\lambda \approx 692$–695 nm immediately followed by a sharp drop in T at $\lambda \approx 703$–720 nm and near-zero T is observed beyond $\lambda \approx 710$ nm, with residual Fabry-Pérot (F-P) oscillations at longer wavelengths attributable to the pore depth. This classic asymmetric shape is a Fano resonance, which happens because the narrow plasmonic modes inside the metal-filled pores interfere with the broad background light passing through the thick silicon substrate [64–66]. Interestingly, changing the pore width from 50 nm to 600 nm changes the transmission intensity but does not shift the absolute zero transmission dip (≈ 710 nm) positions. This trend shows that the resonance frequency is strictly followed by the fixed structural periodicity (Λ = 700 nm), i.e. it is independent of the metal content present in the PSi.

Table 2 Geometrical parameters of one-dimensional porous silicon array for the pore width optimization

w (nm)	Pore thickness (nm)	Pore-filling metals	Λ (Unit Cell width) (nm)	Wavelength Spectrum (nm)
50–600	400	Gold (Au)	700	250–1200
50–600	400	Silver (Ag)	700	250–1200
50–600	400	Coppers (Cu)	700	250–1200

To confirm the propagating character of the resonant mode identified above, we swept the angle of incidence for TM-polarized light from 0° to 6° for each metal and tracked the shift in resonance wavelength (Fig. 4). For Ag, the resonance shifted monotonically from 718 nm at normal incidence to 890 nm at 6°. Au and Cu showed a similar initial shift (710–712 nm to ≈ 865 nm between 0° and 4°) but the resonance position saturated between 4° and 6°, remaining near 865 nm for both angles. This systematic, angle-dependent shift is the classical dispersion signature of a grating-coupled, propagating SPP mode [67–69], and confirms the mode assignment used throughout Sect. "Results and Discussion".

Linewidth Analysis and Critical Coupling

Magnified views of the transmission dips (Figs. 5b, d, f) show the FWHM, which measures how efficiently light couples into the surface plasmon polariton (SPP) modes. A large FWHM indicate poor coupling, where uncoupled light is lost to heat inside the metal or absorbed by the bulk silicon substrate [17, 70]. Under bottom-up illumination, this coupling depends heavily on the type of metal used i.e. Ag has shown sharpest resonance for a wavelength range between 600 and 900 nm. Thanks to its low internal losses, Ag produces the sharpest resonance dip at *w* = 200 nm, outperforming Au and Cu in η (Fig. 5b) [71]. One thing must be kept in mind that the selection of these *w* is not merely restrict to dip sharpness rather their FWHM, E-Norm, η and T_{rel} are also considered which are well described in the incoming sections. For Au critical coupling happens at a wider range of *w* i.e. between 200 nm and 250 nm, with transmission peak at ~ 0.075 a.u. The broadening of dips and hence FWHM for $w \geq 300$ nm is attributable to the inter-band absorption [72, 73]. And in the case of Cu, the optimal coupling shifts to *w* = 250 nm (Fig. 5f) with peak transmission limited to 0.071 a.u. due to the internal damping. At longer wavelengths (750–850 nm), Silver maintains clear transmission oscillations, while Au and Cu flatten out completely due to heavy material absorption. As the calculated absorption enhancement ratio stays above one across

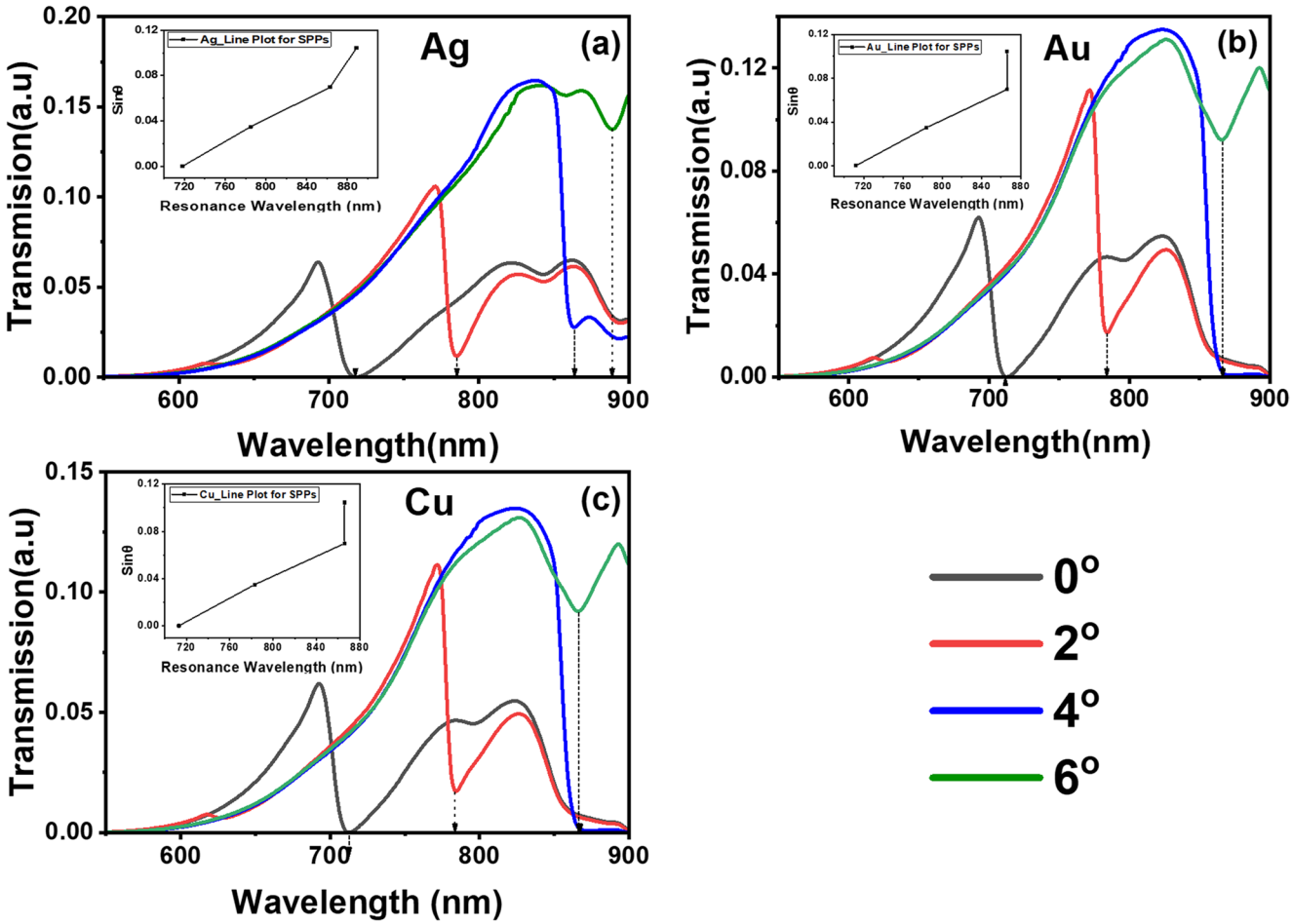


Fig. 4 Angular dispersion of the TM light transmission and inset showing plot between resonance wavelength and sin(θ) for Ag, Au, and Cu, θ = 0°–6°

the spectrum, this grooved design provides a broad optical response rather than working only at a single narrow peak [74, 75]. The extra dips correspond to longitudinal F-P resonances matching the depth of the channels (Figs. 6, 7 and 8). In this regime, the metal-filled pores act as lossy plasmonic waveguides that actively pull in and absorb a major fraction of the incident light within the pillars, rather than just acting as simple scattering centers [76–79].

Resonance Trapping and Waveguiding

The structural design consists of alternating domains of metal and c-Si, where the metallic inclusion widths range from 50 to 450 nm and the c-Si channel widths correspondingly range from 650 to 250 nm. The two domains are inversely coupled i.e. as the metallic inclusion width increases, the c-Si channel width decreases proportionally. This constitutes a hybrid nanocomposite geometry establishing a periodic array of metal-semiconductor-metal interface. This structure strongly supports LSPR and SPPs at the Ag/c-Si boundaries attributed to the high *n* of c-Si. At c-Si width of 250 nm these SPPs hybridizes with the dielectric waveguide modes of the silicon pillars due to the spatial confinement, driving intense near-field concentration into the semiconductor material [80–85]. It should be noted that dips for $w > 450$ nm become too broad to be meaningfully evaluated for FWHM, this is attributed to the high metal content in the pore geometry. Therefore, further analysis is only restricted to a maximum *w* of 450 nm. Widening the *w* continuously from 50 nm to 450 nm causes a small, steady red-shift in the RW from 703 nm to 716–720 nm across all metals (Figs. 9a–c). This happens because expanding the pore changes the effective *n* of PSiA (Tables 3, 4 and 5).

The FWHM behaviour differs across the three metals and must be described individually. For Ag, FWHM remains low and stable in the range 20–55 nm for pore widths up to $w = 250$ nm, then rises gradually to 53, 64, and 65 nm at $w = 300$, 350, and 400 nm, respectively, before spiking sharply to 115 nm at $w = 450$ nm (Table 6). The broadening in Ag is therefore progressive rather than abrupt, reflecting the lower intrinsic damping of Ag that sustains efficient coupling over a wider geometric range. For Au, the transition

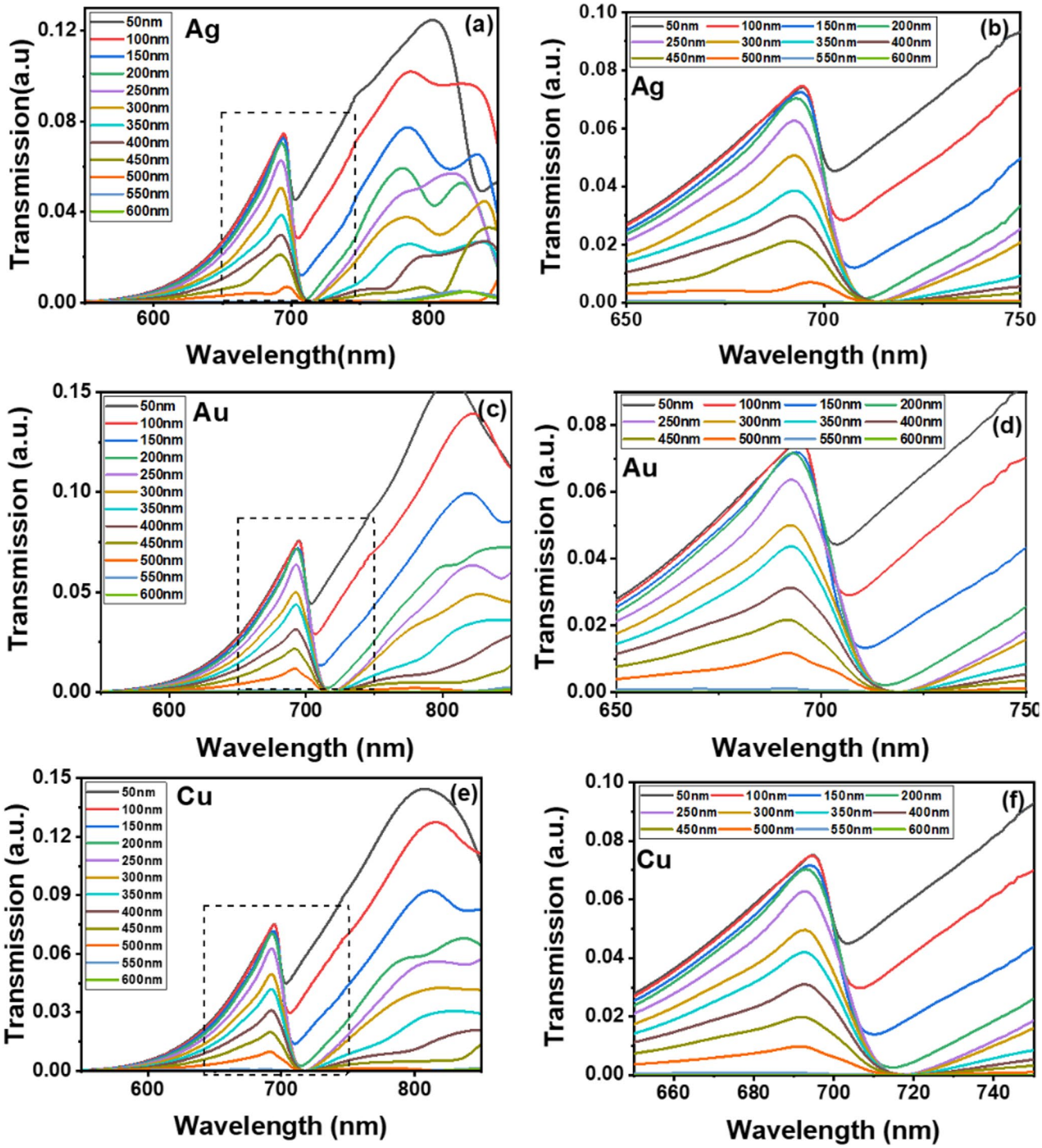


Fig. 5 Transmission plots for transverse magnetic light illuminated on 1D PSiA with Ag (**a**, **b**), Au (**c**, **d**) and Cu(**e**, **f**) can be seen for the pore width ranging from 50 nm to 600 nm for fixed periodicty of 700 nm

is more pronounced: FWHM remains below 65 nm up to $w = 250$ nm but then rises steeply to 90 nm at $w = 350$ nm and exceeds 110 nm at $w = 400$ nm (Table 7), consistent with the onset of inter-band absorption losses in Au above 520 nm. Cu follows a similar trajectory to Au, with FWHM exceeding 85 nm at $w = 350$ nm and 108 nm at $w = 400$ nm (Table 8), reflecting its higher ohmic damping. In all three metals, the FWHM exceeding approximately 100 nm signals breakdown of critical coupling, at which point the system transitions from a resonance-trapping regime to one

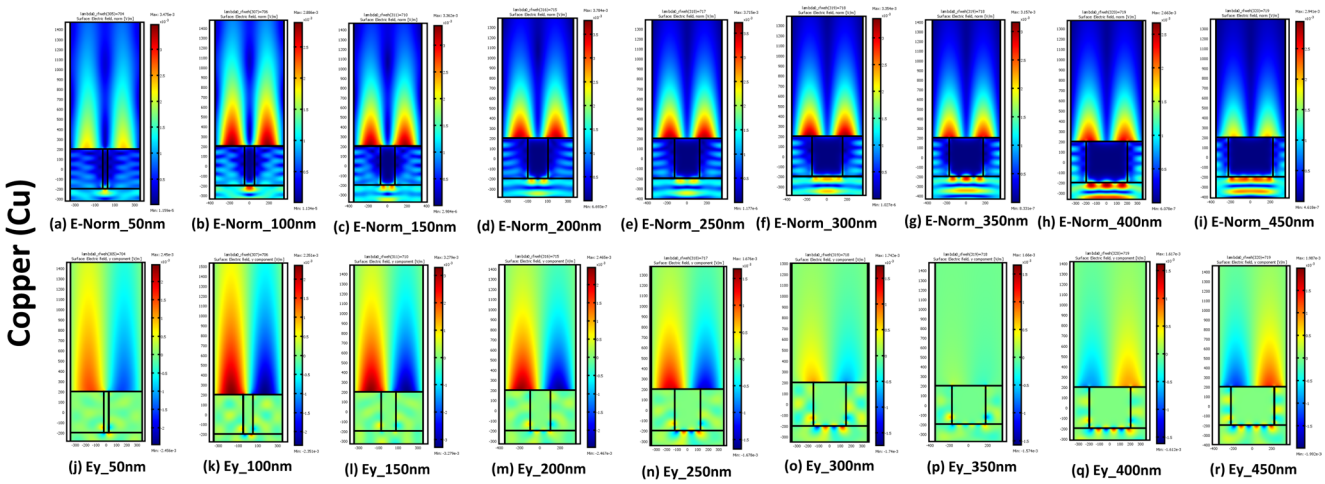


Fig. 6 Surface plots of the E_y field component and E-Norm, illustrating the spatial field distribution at the Ag/air and Ag/Si interfaces for w ranging from 50 nm to 450 nm at a fixed Λ of 700 nm

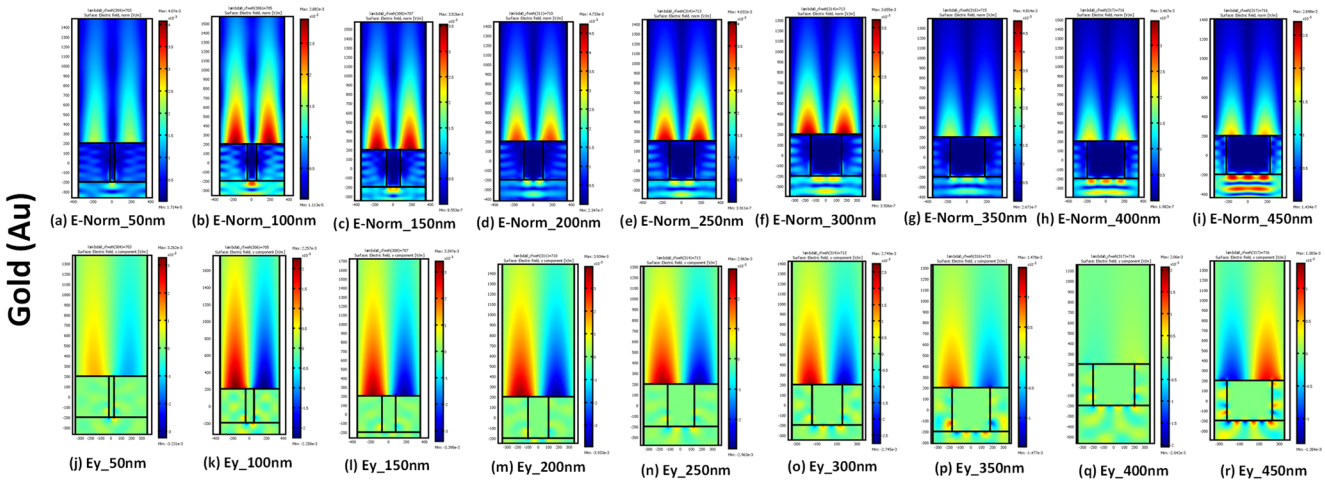


Fig. 7 Surface plots of the E_y field component and E-Norm, illustrating the spatial field distribution at the Au/air and Au/Si interfaces for w ranging from 50 nm to 450 nm at a fixed Λ of 700 nm

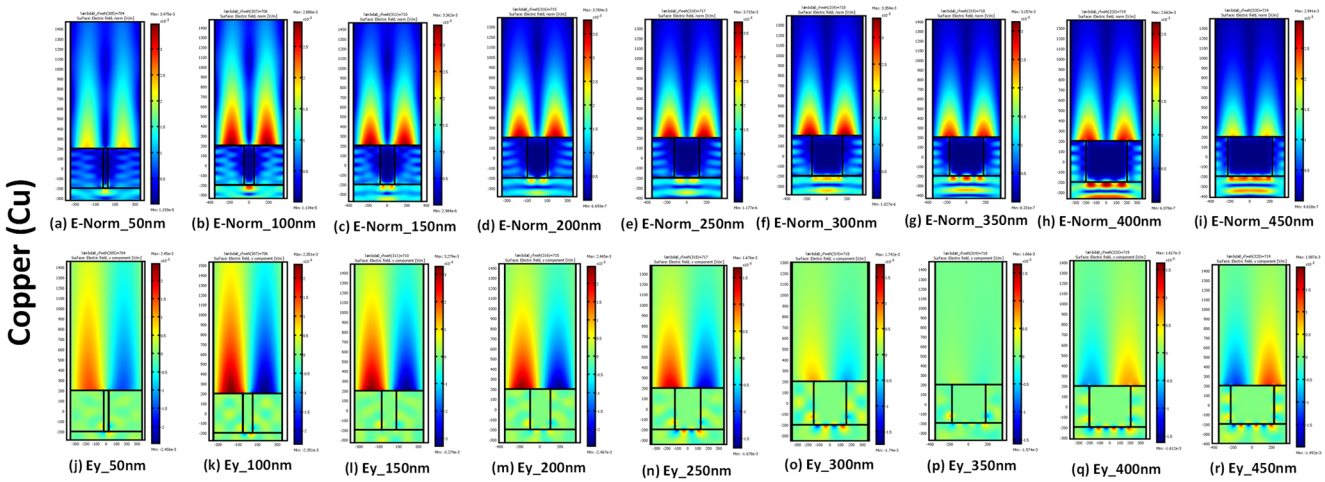


Fig. 8 Surface plots of the E_y field component and E-Norm, illustrating the spatial field distribution at the Cu/air and Cu/Si interfaces for w ranging from 50 nm to 450 nm at a fixed Λ of 700 nm

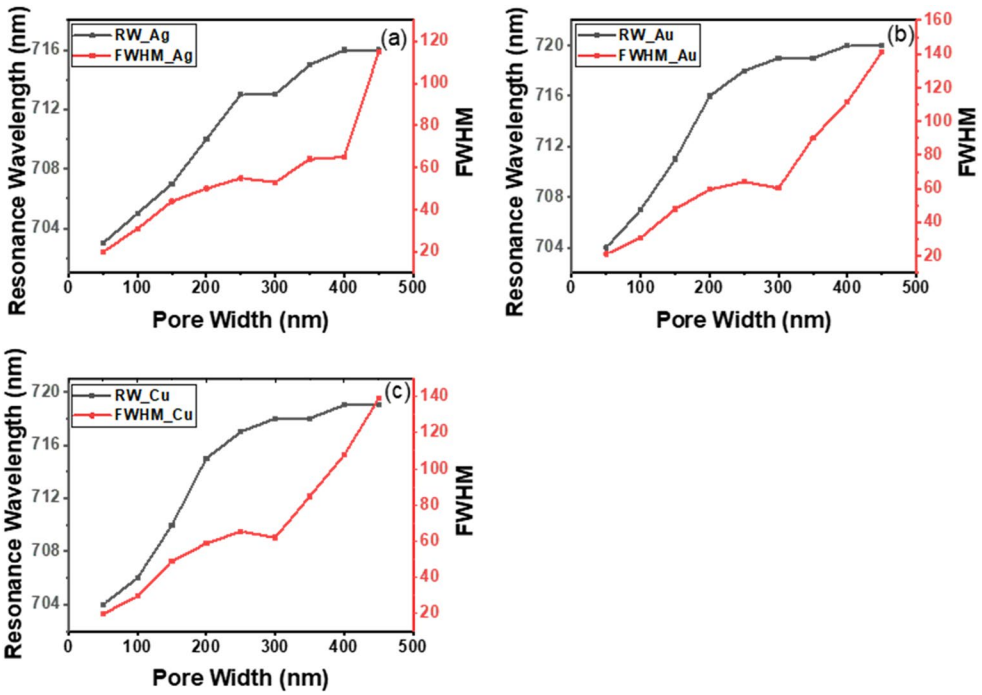


Fig. 9 Correlation between resonance wavelength (RW) and Full width at half maximum (FWHM) for pore width (w) optimization range (50–450 nm) for PSiA showing the quasi-linear relation of w with RW and FWHM (**a**) Ag, (**b**) Au, and (**c**) Cu

Table 3 Coupling efficiency (η) and relative transmission (Trel) of TM-polarized light extracted from Fig. 12, for pore width optimization in the Ag-filled 1D PSiA at a fixed periodicity Λ = 700 nm

Sr. no.	w (nm)	RW (nm)	AB	AB/AC	T_2 (TE)	T_1 (TM)	$T_{rel} = T_1 - T_2$	η=(AB/AC)100%
1	50	703	0.02989	0.39778	0.069817	0.074269	0.004452	39.7779681
2	100	705	0.03534	0.554526	0.05769	0.074539	0.016849	55.4526423
3	150	707	0.04654	0.794608	0.051369	0.072452	0.021084	79.4607916
4	200	710	0.050947	0.972423	0.044761	0.070333	0.025573	97.2423473
5	250	713	0.035557	0.997708	0.033543	0.06258	0.029037	99.7707568
6	300	713	0.029163	0.990997	0.026041	0.050521	0.024479	99.0997402
7	350	715	0.025806	0.999151	0.021688	0.038568	0.01688	99.9150943
8	400	716	0.032981	0.999354	0.022742	0.029815	0.007072	99.935361
9	450	716	0.019836	0.999798	0.017258	0.021159	0.003901	99.9797583

Table 4 Coupling efficiency (η) and relative transmission (Trel) of TM-polarized light extracted from Fig. 13, for pore width optimization in the Au-filled 1D PSiA at a fixed periodicity Λ = 700 nm

Sr. no.	w (nm)	RW (nm)	AB	AB/AC	T_2 (TE)	T_1 (TM)	$T_{rel} = T_1 - T_2$	η=(AB/AC)100%
1	50	704	0.0339	0.433497	0.071399	0.075908	0.004509	43.3496975
2	100	707	0.036764	0.558366	0.058014	0.075537	0.017523	55.8366152
3	150	711	0.049147	0.786872	0.051639	0.072011	0.020373	78.6871944
4	200	716	0.056212	0.96362	0.0453	0.071761	0.026461	96.3619779
5	250	718	0.038875	0.999267	0.034615	0.063784	0.029169	99.926717
6	300	719	0.032284	0.998191	0.025287	0.050083	0.024795	99.8190931
7	350	719	0.027067	0.999109	0.021504	0.043744	0.02224	99.9108943
8	400	720	0.035209	0.999516	0.022212	0.031362	0.009149	99.9516272
9	450	720	0.022494	0.999219	0.018726	0.021737	0.003011	99.9218622

dominated by radiative scattering leakage and conduction losses [86]. The onset of this transition occurs at $w \geq 300$ nm for Au and Cu and at $w \geq 400$ nm for Ag, confirming that Ag sustains tighter resonance control over a broader geometric window.

To isolate the effect of the metal itself, we compared the transmission spectrum of the metal-filled structure against an identical pore geometry without metal (Fig. 10a). The empty-pore control transmits freely beyond 750 nm, exceeding 0.2 by 900 nm, while the Ag-, Au-, and Cu-filled structures suppress

Table 5 Coupling efficiency (η) and relative transmission (Trel) of TM-polarized light extracted from Fig. 15, for pore width optimization in the Cu-filled 1D PSiA at a fixed periodicity Λ = 700 nm

Sr. no.	w (nm)	RW (nm)	AB	AB/AC	T_2 (TE)	T_1 (TM)	$T_{rel}= T_1-T_2$	η=(AB/AC)100%
1	50	704	0.0328	0.42145150	0.0711	0.0752	0.00412	42.1451509
2	100	706	0.0186	0.28712413	0.0576	0.0749	0.01728	28.7124132
3	150	710	0.0474	0.77283830	0.0515	0.0716	0.02008	77.2838300
4	200	715	0.0544	0.95378151	0.0451	0.0703	0.02523	95.3781512
5	250	717	0.0382	0.99736032	0.0338	0.0626	0.02877	99.7360328
6	300	718	0.0317	0.99936915	0.0253	0.0494	0.02418	99.9369158
7	350	718	0.0265	0.99803581	0.0210	0.0418	0.02087	99.8035815
8	400	719	0.0340	0.99898145	0.0226	0.03096	0.00831	99.8981459
9	450	719	0.0218	0.99842646	0.01838	0.0199	0.00152	99.8426459

Table 6 Statistical details of FWHM, peak E-Norm, T_{rel} and η profiles as a function of w for an Ag-filled 1D PSiA plotted in Fig. 14(a-b)

Sr. no.	w (nm)	FWHM	E-Norm	$T_{rel} = T_1-T_2$	η = (AB/AC)100%
1	50	20	0.00234	0.004452	39.7779681
2	100	31	0.00288	0.016849	55.4526423
3	150	44	0.00345	0.021084	79.4607916
4	200	50	0.0044	0.025573	97.2423473
5	250	55	0.00415	0.029037	99.7707568
6	300	53	0.003734	0.024479	99.0997402
7	350	64	0.00289	0.01688	99.9150943
8	400	65	0.0024	0.007072	99.935361
9	450	115	0.00196	0.003901	99.9797583

Table 8 Statistical details of FWHM, peak E-Norm, T_{rel} and η profiles as a function of w for a Cu-filled 1D PSiA plotted in Fig. 14(e-f)

Sr. no.	W (nm)	FWHM	E-Norm	$T_{rel} = T_1-T_2$	η = (AB/AC)100%
1	50	19.56224	0.0024	0.00412	42.14515093
2	100	29.3434	0.0029	0.01728	28.71241326
3	150	48.90561	0.0033	0.02008	77.28383
4	200	58.68673	0.0039	0.02523	95.37815126
5	250	65.20748	0.004	0.02877	99.73603282
6	300	61.9471	0.0034	0.02418	99.93691588
7	350	84.76972	0.0031	0.02087	99.80358152
8	400	107.5923	0.0027	0.00831	99.89814591
9	450	138.9421	0.0021	0.00152	99.84264596

transmission to approximately 0.05–0.065 across the same range. This confirms that the metal is responsible for intercepting a substantial fraction of the incident light at these wavelengths, consistent with the SPP-mediated absorption mechanism established as beneficial for plasmon-enhanced photocatalysis.

Figure 10 (b) is the postprocessing of the model showing the Poynting-vector energy-flow maps. The periodic fringe pattern in the silicon region is consistent with a Fabry-Pérot-type cavity contribution, since reflection- and interference-based optical modes in thin-film silicon are governed primarily by layer geometry and boundary conditions [87]. The localized field reversal at the pore corner further supports a dipolar plasmon interpretation, because dipole plasmon resonances are expected to produce characteristic local-field structure near the metal feature [88].

Near Field Trapping in Metal-Filled Nanopores

It is the analysis of electromagnetic fields close to the plasmonic interfaces ($r << \lambda$), which captures non-propagating evanescent waves to evaluate highly localized energy distributions and hot-spots at the material boundaries. Figures 11a, c, and e show spatial line-scans across the periodic domain, where the peaks represent the relative local electric field with respect to the incident source field. The sharp peak discontinuities correspond to localized field confinement at the geometric boundaries of the metal/c-Si interfaces, while the broader, smoother field distributions represent the spatial profile of propagating SPP modes within the adjacent semiconductor channels [89–92]. To evaluate the light-trapping mechanism within the metal-filled pores, the E-Norm

Table 7 Statistical details of FWHM, peak E-Norm, T_{rel} and η profiles as a function of w for an Au-filled 1D PSiA plotted in Fig. 14(c-d)

Sr. no.	W (nm)	FWHM	E-Norm	$T_{rel} = T_1-T_2$	η = (AB/AC)100%
1	50	21.21	0.00234	0.004509	43.3496975
2	100	30.93	0.00316	0.017523	55.8366152
3	150	47.88	0.00394	0.020373	78.6871944
4	200	59.47	0.00452	0.026461	96.3619779
5	250	64.09	0.00455	0.029169	99.926717
6	300	60.41	0.00345	0.024795	99.8190931
7	350	89.98	0.003	0.02224	99.9108943
8	400	111.54	0.00265	0.009149	99.9516272
9	450	141.35	0.00211	0.003011	99.9218622

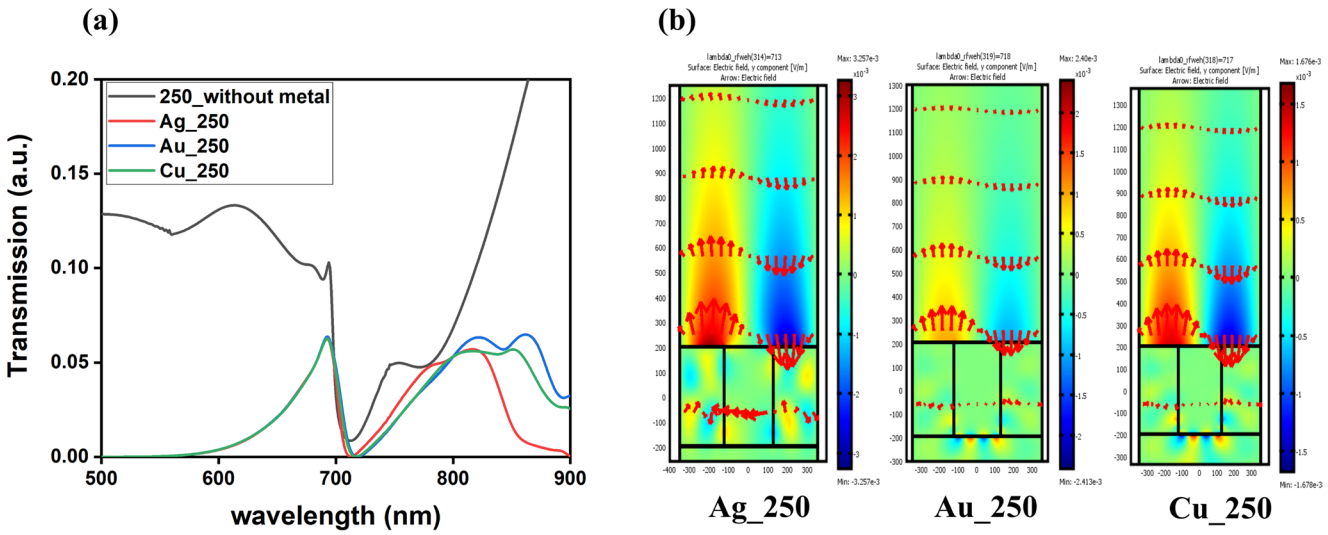


Fig. 10 (**a**) Transmission spectra at w = 250 nm for the empty pore array (no metal) versus Ag-, Au-, and Cu-filled pores (**b**) Poynting-vector energy flow maps for Ag, Au, Cu at their respective resonance wavelengths

(|E|) was collected via COMSOL Multiphysics. Figures 11(a, c, e) display the spatial field profiles across a 700 nm sweep (from − 350 nm to + 350 nm) for Ag, Au, and Cu across varying w. All profiles exhibit strict spatial symmetry characterized by a distinct intensity minimum at the pore center (0 nm). Narrow pores (50–150 nm) show low field intensity. There are several design approaches to maximize field confinement like Nanogap, Tip enhancement, Core-shell, periodic array [23] and our geometry falls in the category periodic arrays. As we know that LSPR occurs when d<< λ, that's why as the width approaches critical coupling, the LSPR create sharp hot-spots near the metal-dielectric corners (± 100 nm to ± 250 nm) across all the metals. For Ag (Fig. 11a), this peaks at exactly $w = 200$ nm with a maximum field value of 0.0044 a.u. due to its low imaginary permittivity (ε_2) and minimal internal losses [93, 94]. A more precise characterization of the LSPR peak position would require Surface-enhanced Raman Spectroscopy (SERS) measurements, which are beyond the scope of this computational study and are proposed as a future direction. Figure 11(b, d, f) shows the line plot of electric field with respect to pore width for Ag, Au and Cu filled PSi. Figure 11(b) shows the plot for Ag where we can see a monotonic increase in electric field from 50 nm, establishing a single highly resolved maxima at $w = 200$ nm. Thanks to lower imaginary permittivity of Ag in that spectral window that is the reason for optimal impedance matching and minimal parasitic damping. Beyond $w = 200$ nm, the peak field strength drops sharply, which corresponds to the broadening of line width that takes the structure into a radiation-dominant damping regime [95]. A flatter, broadened plateau can be seen from Fig. 11(d) for Au shows $w = 200$ to 250 nm, reaching a maximum of relative field to approximately 0.0045 a.u. This is the indication of a wider geometric coupling regime that appears as secondary sharp field spikes close to ± 100 nm for the 200 nm and 250 nm pore sweeps (Fig. 11c). This is consistent with the known inter-band transitions in Au at ~ 2.4 eV (~ 520 nm), which perturb localized spatial charge displacement [96]. Figure 11(f) shows the plot for Cu that shows a peak at $w = 250$ nm with a somewhat lower value of 0.0040 a.u. with respect to Ag and Au. This shift is an explicit physical consequence of the elevated conduction path losses and severe electronic damping characteristic of Cu, that requires a larger slot volume to sustain comparable gap-plasmon field confinement [97].When the pore width exceeds 400 nm, the field profile flattens and drops heavily across all metals. This decay supports that higher value of metal content decouple the plasmonic walls, allowing the electromagnetic energy to leak radiatively into the surrounding environment rather than remaining trapped along the active metallic walls [98].

Coupling Efficiency and Relative Transmission

When TM light illuminates the 1D PSiA through the c-Si substrate, SPPs are excited at the metal/c-Si and metal/air interfaces. These excited modes constructively interfere with incident light, causing a sharp transmission dip followed by enhanced resonant peaks [16]. TE light cannot excite SPPs because its electric field lacks a component perpendicular to the metallic walls. We can express the phase-matching condition for grating-coupled SPP excitation as:

$$k_g = \triangle k_x = \frac{2\pi}{\Lambda} \tag{4}$$

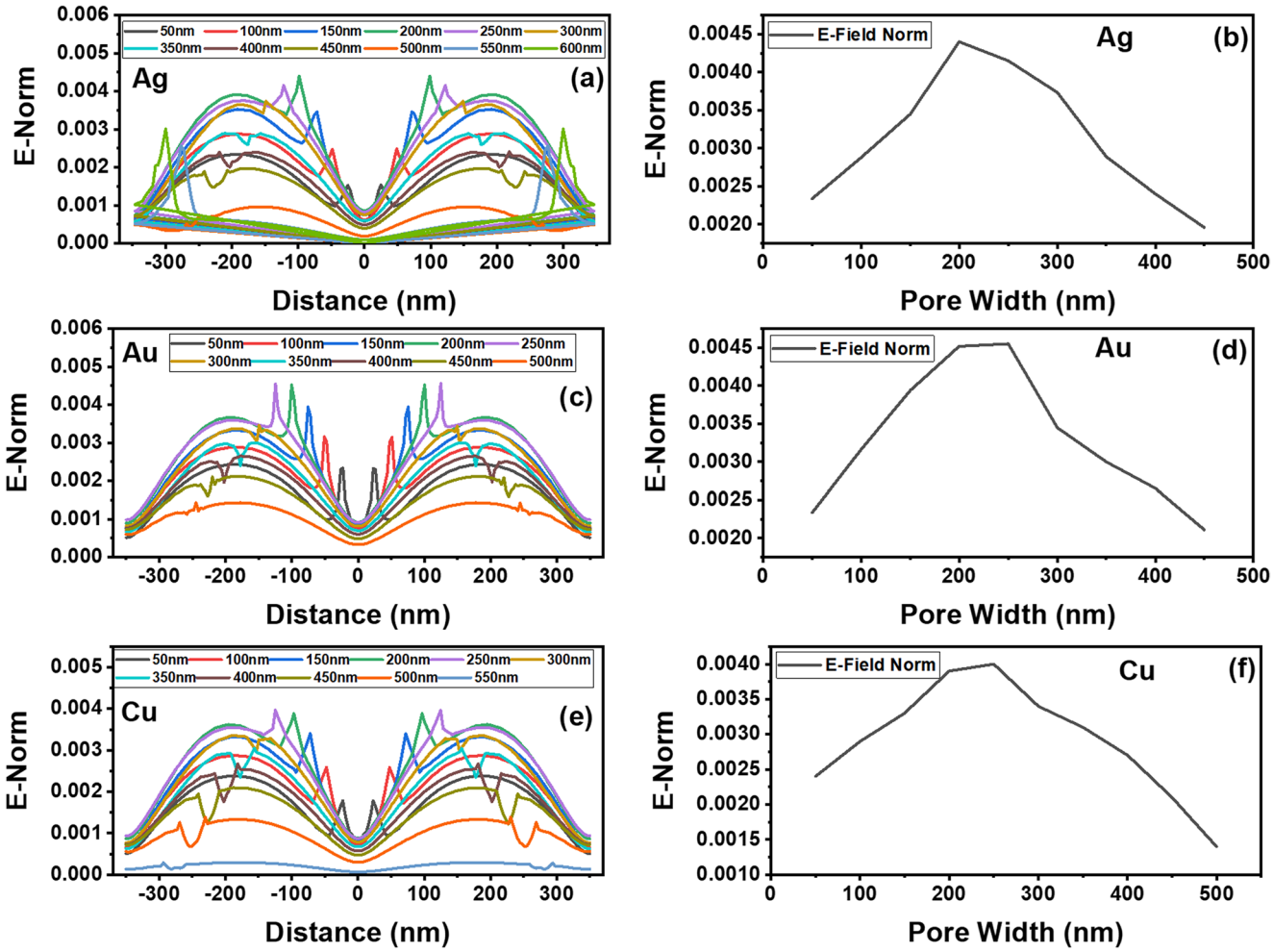


Fig. 11 The E-Norm distribution along the spatial distance coordinate (-350 nm to +350 nm) of pore width (w) optimization for (**a**) Ag, (**c**) Au, and (**e**) Cu. Corresponding peak E-Norm variations plotted directly as a function of w to identify the optimized geometric constraints for (**b**) Ag, (**d**) Au, and (**f**) Cu

Here Λ represents, as before, the grating periodicity. This should be considered that moving away from F-P resonances, η increases for longer wavelengths [17, 99–102]. Far-field analysis reveals that the resonance dip deepens significantly when the w spans 2/7 to 1/3 of the Λ under normal incidence ($\theta_i = 0°$), signaling maximized light absorption and localized energy coupling. There are two ways to quantify this plasmonic interaction:

i. Coupling Efficiency: We assess the magnitude of the TM transmission dip relative to a baseline lacking SPP excitation:

$$\eta = \left(\frac{AB}{AC}\right) \times 100\% \tag{5}$$

where B is the transmission minimum at the TM resonance dip, A is the baseline TE transmission at the same wavelength, and C is the unchanged transmission intensity reference [16, 17].

ii. Relative Transmission: It accounts for the far-field impact of SPP generation by calculating the difference between the TM interference peak (T_1) and baseline TE transmission (T_2) at the resonance RW [103, 104].

$$T_{rel} = T_1 - T_2 \tag{6}$$

Coupling Efficiency and Relative Transmission of Ag

To evaluate the performance of the Ag-filled PSiA, Fig. 12 plots the transmission curves for TM and TE polarization, alongside their respective η and T_{rel} values calculated via Eq. 5 and Eq. 6. Sweeping the w from 50 to 450 nm reveals that both metrics depend strongly and non-linearly on the sub-wavelength channel geometry at each resonance wavelength [16, 105], as detailed in Table 3. The η rises from 39.78% at w = 50 nm to 97.24% at the critical coupling threshold of w = 200 nm. This rise is consistent with the previously

established far field and near-field behavior of PSiA at the said w.

For the $w = 250$ nm, the η reaches into a distinct saturation regime, hence, maintaining an elevated baseline of η ≈ 99.10% to 99.98% through the upper limit of $w = 450$ nm. It should be noted that these are numerical results and in a fabricated device, η would be somewhat lower attributed to geometric imperfections and additional loss mechanisms. Thus a geometric saturation of η does not, however, always produce a corresponding enhancement in optical performance [61]. Tracking the relative transmission ($T_{rel} = T_1 - T_2$), a clear divergence from the η profile can be seen. The T_{rel} increases steadily to a peak value of 0.0290 a.u. at $w = 250$ nm and then undergoes a continuous, severe degradation down to 0.0039 a.u. at $w = 450$ nm (Fig. 14 (b)).

This behaviour arises because at $w > 250$ nm the ideal cavity configuration breaks down. Even though these wider pores catch most of the incoming light momentum and couple with it almost perfectly, they cannot hold onto it. The phase-matching conditions change, forcing the light to either

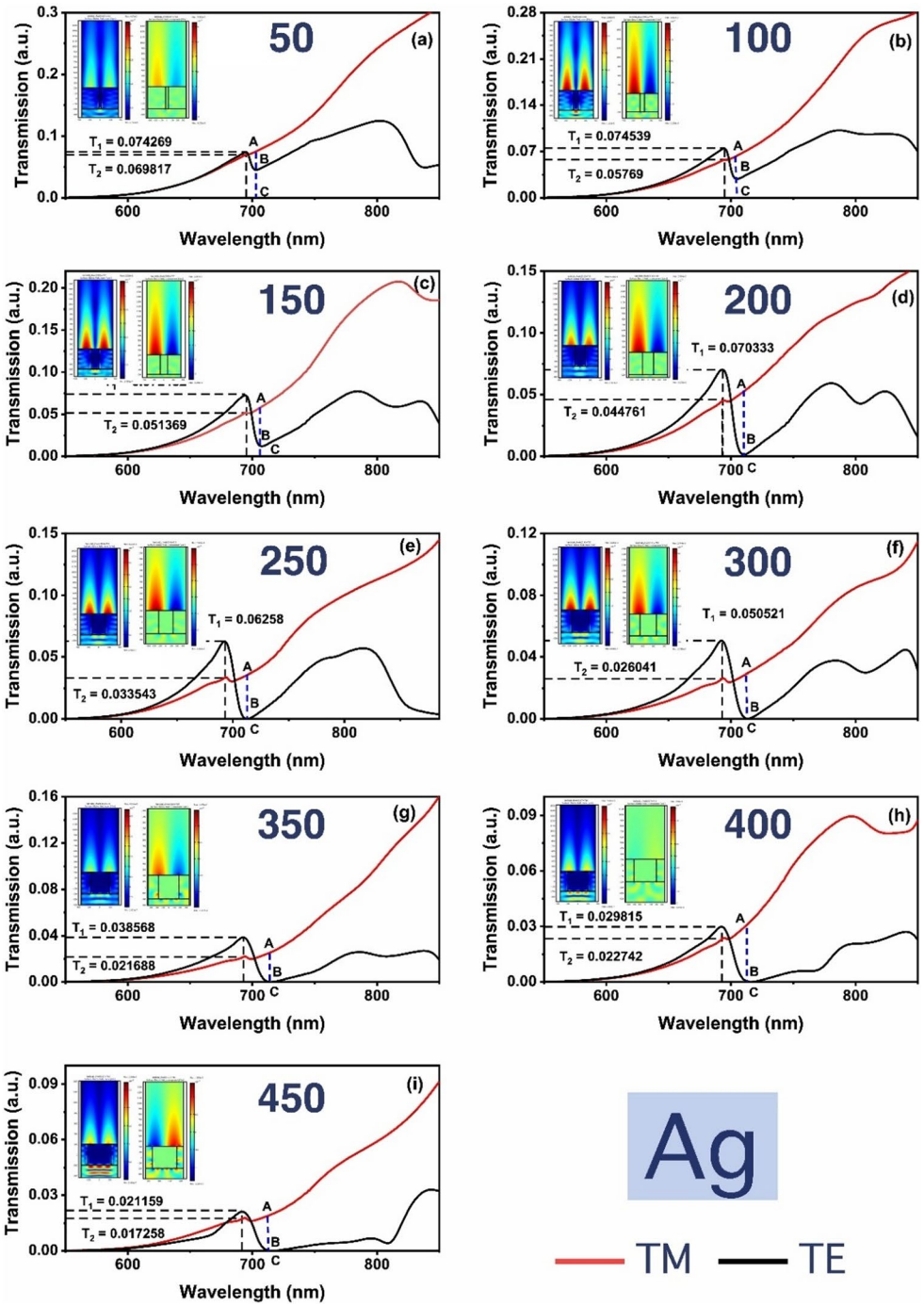


Fig. 12 Coupling efficiency and Relative transmission of Ag-filled 1D PSiA as a function of *w* ranging from 50 nm to 450 nm at a fixed periodicity Λ = 700 nm

scatter away into the air or die out as heat inside the metal [106]. Therefore, trapped electromagnetic energy inside the oversized pores escapes via uncoupled radiative leakage or is dissipated by severe ohmic conduction losses along the extended metal boundaries rather than contributing to the forward transmission. For photovoltaic and light-harvesting applications, these trends indicate that maximizing performance requires prioritizing the narrow w = 200 to 250 nm window, where the ideal balance between energy trapping and forward transmission is preserved [107, 108].

The surface plots of the E-Norm and the vertical field y-component (E_y) of Ag presents the F-P resonance as shown in Fig. 6.

Coupling Efficiency and Relative Transmission of Au

A similar sweep of w, along with the calculation of η and T_{rel} was carried out for Au as well shown in Fig. 13, revealing that, this Au filling present inside the PSi support LSPR fields whose strength and RW depend on the pore size and morphology [109–111]. Table 4 details the calculated values of η and T_{rel}, which exhibit a trend similar to that of Ag i.e. both η and T_{rel} rise simultaneously until critical coupling is achieved. Beyond this point, η saturates near unity while T_{rel} drops abruptly. Notably, Au demonstrates a high initial η of 43.35% at w = 50 nm, outperforming Ag despite the intrinsic d-band transitions present in Au within the visible spectrum (Fig. 14 (d)). This again demonstrates that high η does not guarantee high performance.

At an optimal width of w = 250 nm, the system balances light trapping and transmission. Beyond w > 300 nm, despite near-perfect coupling (≈ 99.9%), T_{rel} collapses as disrupted waveguide conditions redirect energy into radiative scattering and parasitic gold inter-band absorption [111, 112]. Consequently, a 200–250 nm width is recommended for light-harvesting applications.

The Surface plots of the E-Norm and E_y of Au illustrate an F-P resonance as shown in Fig. 7.

Coupling Efficiency and Relative Transmission of Cu

Analogous parametric sweeps and calculations of η and T_{rel} were performed for Cu as shown in Fig. 15. The coupling efficiency follows a nearly linearly increasing trend that is enhanced coupling with η reaching 95.38% for w=200 nm and attaining saturation at w=250 nm (Table 5).

Cu also shows a trend analogous to Ag and Au in T_{rel} i.e. it rises simultaneously until critical coupling is achieved. Beyond this point, η saturates near unity while T_{rel} drops abruptly till 450 nm slit width. And this drop in T_{rel} is attributed to EM energy absorption occurring in non-radiative inter-band transitions and parasitic ohmic losses along the metal boundaries [113]. Hybrid metal-semiconductor-metal designs can reduce ohmic loss while keeping strong confinement [81, 113, 114]. Cu plasmonic waveguide can show unexpectedly low propagation losses and efficient coupling when geometries are engineered carefully, even outperforming Au in some CMOS-compatible slot configurations [115, 116]. For practical light-harvesting devices, these results prove that the w = 200 to 250 nm window is essential to overcome Cu's high material damping and ensure maximum forward optical transfer.

The F-P resonance of the Cu can be seen from the surface plots of the E-Norm and E_y as shown in Fig. 8.

Correlation of Near-Field and Far-Field Patterns, Coupling Efficiency, and Relative Transmission

A correlation is established between near-field and far-field analyses, which is standard practice for validating simulation results, since far-field outputs should be consistent with near-field observations. This correlation is characterized as a curve plotted with w along the horizontal axis and FWHM (far-field) and E-Norm, near-field along the vertical axes, as shown in Fig. 14 (a, c, e) for all three metals investigated, namely Ag, Au, and Cu and their respective tables are also listed below as Tables (6, 7, 8). The selection criterion is that only those w are chosen for which the highest value of the E-Norm corresponds to a FWHM that falls within its minimum values.

For the Ag-filled PSiA, the highest value of E-Field Norm is observed at w=200 nm (Fig. 14(a)). For the Au-filled PSiA, a plateau is witnessed for the highest value of E-Field Norm in the w range of 200 nm to 250 nm, and both these values of w correspond to marginally similar FWHM values from the lower regime (Fig. 14(c)). Similarly, for Cu-filled PSiA, the E-Field Norm attains its highest value at w=250 nm, with another closely comparable value at w=200 nm. Both these pore widths exhibit corresponding FWHM values from their minimum range (Fig. 14(e)). Therefore, this near-field and far-field correlation across all three metals isconsistent with w=200 nm for Ag, w=200–250 nm for Au, and w=200–250 nm for Cu are the optimized w and ranges for enhanced coupling and energy storage for light harvesting applications. This property of metal-filled PSi structures can be exploited in the fabrication of plasmonic solar cells. A second correlation can be established to further verify and validate these optimization parameters, namely the correlation between η and T_{rel}. This correlation is plotted with w along the horizontal axis and both η and T_{rel} along the vertical axis, as seen in Fig. 14 (b, d, f). These plots further support the correlation results obtained from the FWHM and E-Field Norm analysis. Specifically, both η and T_{rel} increase quasi-linearly with pore width up to a critical coupling threshold, i.e., w=200 nm for Ag and w=250 nm for both Au and Cu.

The T_{rel} starts to decrease after these critical values and this is consistent with the trend observed in the E-Norm

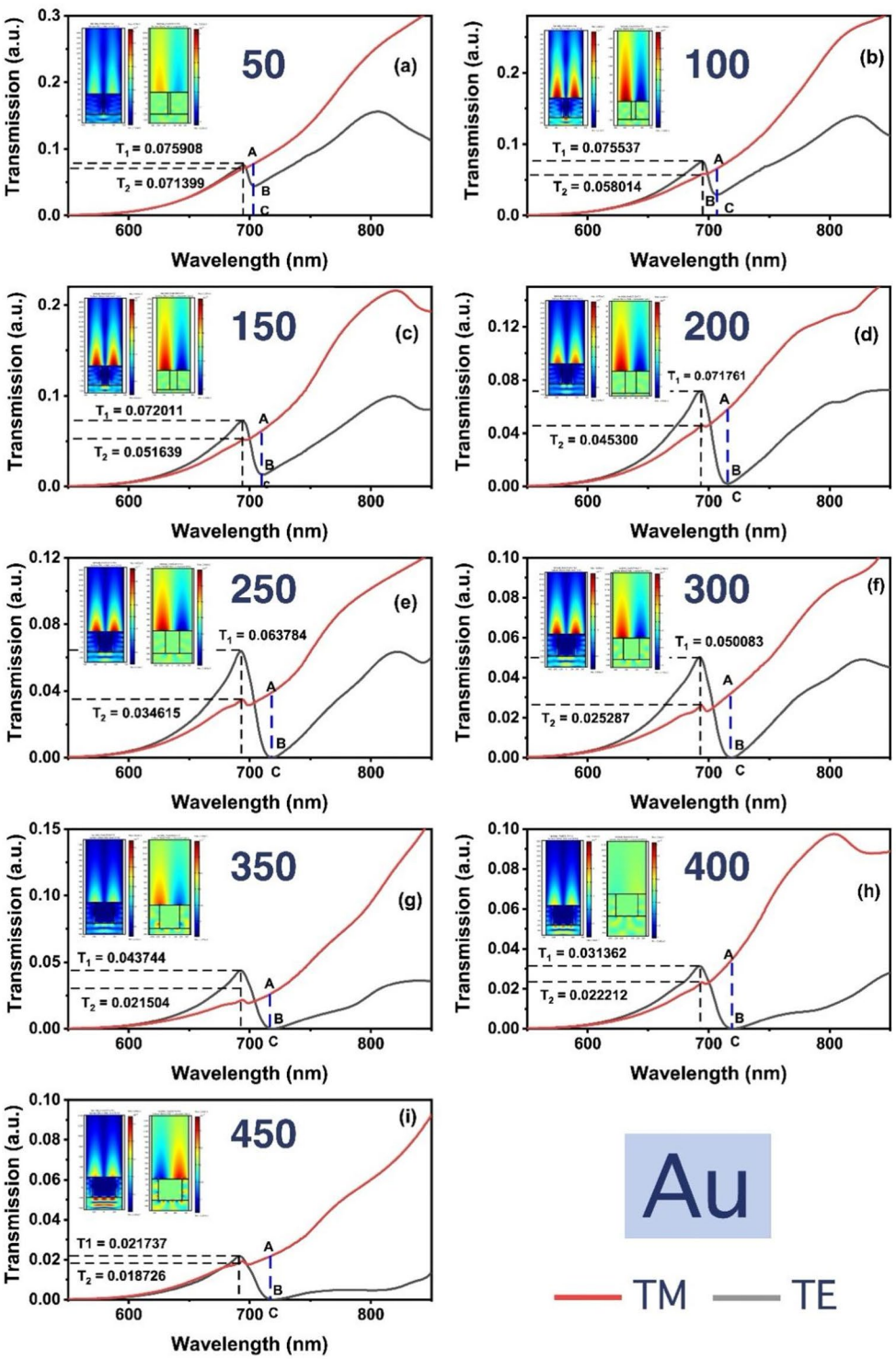


Fig. 13 Coupling efficiency and Relative transmission of Au-filled 1D PSiA as a function of w ranging from 50 nm to 450 nm at fixed periodicity $\Lambda = 700$ nm

in the near-field analysis. These correlations is consistent with the optimized pore widths and ranges for enhanced field trapping and light harvesting are $w = 200$ nm for Ag, $w = 200–250$ nm for Au, and $w = 200–250$ nm for Cu. These tailored PSi architectures hold significant potential for integration into high efficiency plasmonic solar cells.

The reported η and Trel quantify grating-coupled SPP excitation efficiency and do not distinguish useful absorption in c-Si from parasitic ohmic loss in the metal; consequently, the present results should be interpreted as an optical light-trapping design rule rather than a direct prediction of solar-cell efficiency.

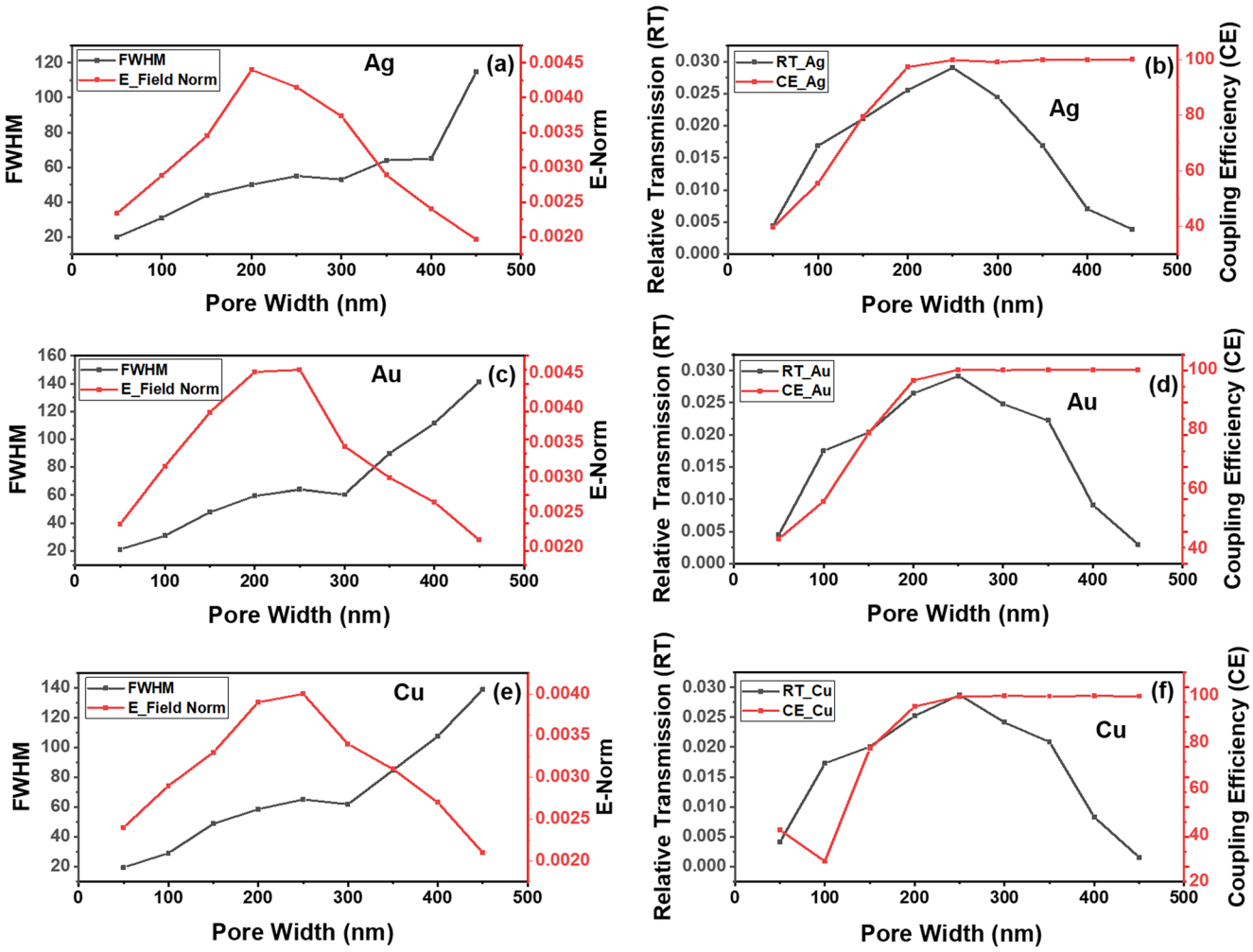


Fig. 14 The four-way correlation of E-Norm (Near field) and FWHM (Far-field) Patterns with respect to pore width for Ag (**a**), Au (**c**), and Cu (**e**); in comparison with their coupling efficiency and relative transmission of Ag (**b**), Au (**d**), and Cu (**f**)

Conclusion

The present study, performed using COMSOL Multiphysics RF Module (v.5.3a), presents a systematic FEA investigation of 1D PSiA for plasmonic light trapping. The simulations are performed for the Ag, Au and Cu filled c-Si (substrate) for w range of 50–600 nm at a fixed $\Lambda = 700$ nm. To the authors' knowledge, this pore-confined, side-by-side FEA comparison of Ag, Au and Cu in c-Si substrate has not been previously reported.

Far-field transmission spectra show a Fano-resonance in the range 703–720 nm across all the metals investigated, arising from the Λ. Due to the progressive change in effective n of PSiA, there is a redshift of approximately 13–17 nm with w changing from 50 to 450 nm.

Near-field spectra (E-Norm) is consistent with the localized field enhancement at the MIS edges of the pores indicating the excitation of LSPR. For Ag E-Norm peaked (0.0044 a.u.) at $w = 200$ nm and for Au and Cu peaked (0.0045a.u. & 0.0040 a.u.) at $w = 200$ nm and 250 nm respectively. This lower value for Cu is a consequence of its interband transition and ohmic damping.

η and T_{rel} are correlated with FWHM and E-Norm exhibiting; $\eta > 95\%$ (97.2% for Ag, 96.4% for Au, and 95.4% for Cu) at $w = 200$ nm for all three metals used and saturates to 99% for $w \geq 250$ nm. Whereas, T_{rel} peaked (~ 0.029 a.u.) at $w = 250$ nm, before, sharp decrease across the metals showing that highest η does not mean highest optical throughput. This divergence of η and T_{rel} demonstrate that oversized pore cannot confine the trapped energy despite momentum matching, hence, dissipating it in ohmic losses and radiative leakage.

A four-way correlation of FWHM, E-Norm, η, and T_{rel} shows that the optimized w for the Ag is 200 nm and for Au and Cu range from 200 to 250 nm, approximately one-third of Λ. This ratio matches the design rule reported for a surface-deposited grating on a-Si [17], despite the present structure differing in host substrate (c-Si vs. a-Si), confinement geometry

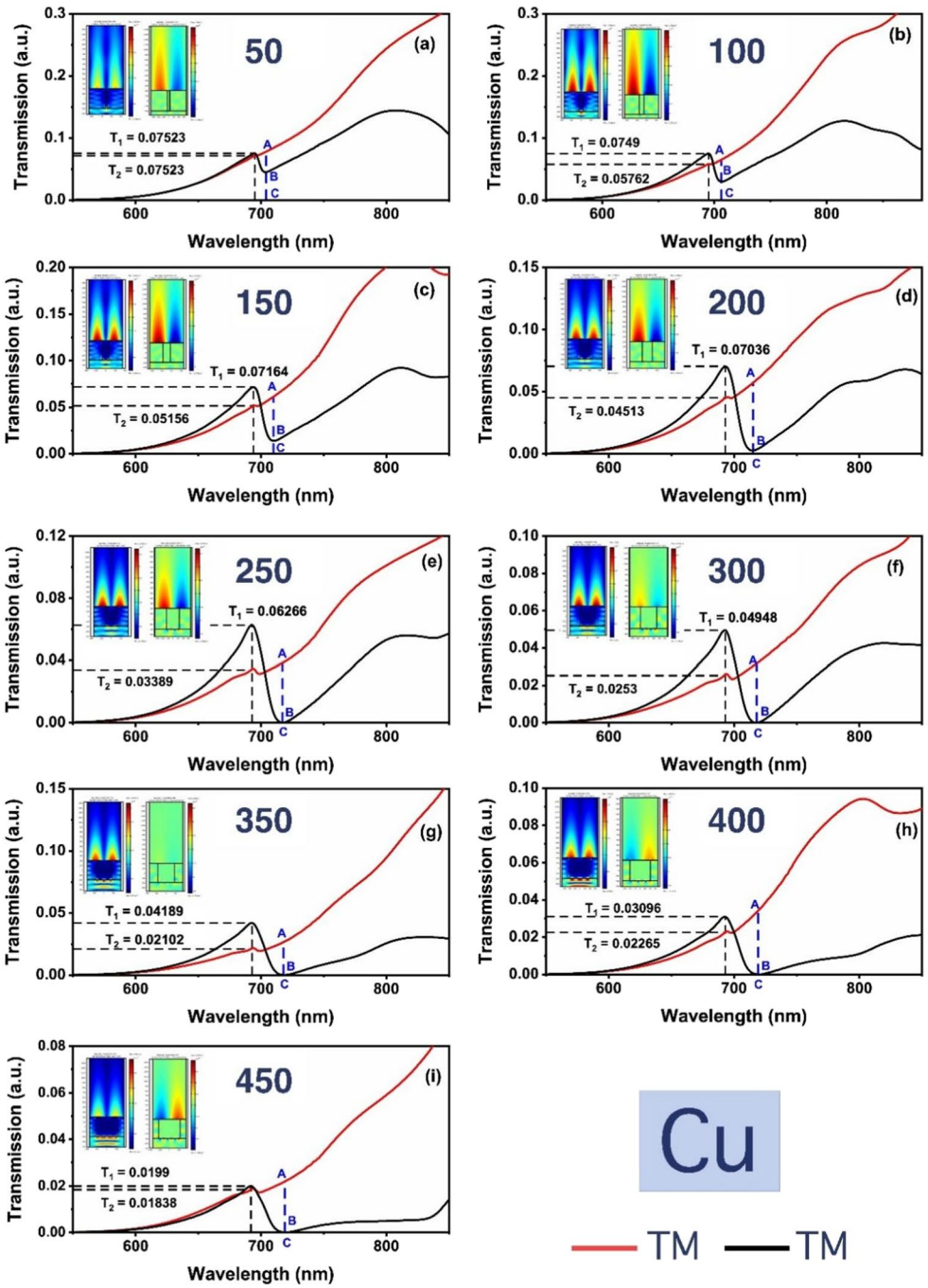


Fig. 15 Coupling efficiency and Relative transmission of Cu-filled 1D PSiA as a function of *w* ranging from 50 nm to 450 nm at a fixed periodicity $\Lambda = 700$ nm

(pore-confined vs. surface deposited), and metal (Ag/Au/Cu vs. Au/Ag only). The persistence of this ratio across these simultaneous changes indicates that w/ $\Lambda \approx 1/3$ is set primarily by grating diffraction condition (Eqs. 1–2) rather than by material-specific parameters, extending the rule's applicability rather than merely reproducing it. Distinct to the pore-confined geometry, however, is the excitation of propagating SPPs along the metal walls and LSPR at the pore corners.

Present results provide a computationally validated design framework for the fabrication of metal-filled PSi plasmonic solar cells. We express that the optimized pore widths of 200–250 nm are compatible with standard electrochemical etching and metal deposition processes, making the proposed architecture practically configurable. We want to extend that the future work should focus on potential directions like:

- The extension of the FEA model to two-dimensional pore arrays and oblique-incidence illumination to assess angular robustness and polarization sensitivity.
- The experimental fabrication and optical characterization of Ag-, Au-, and Cu-filled 1D PSiA structures at the optimum w to validate the simulation predictions.
- The integration of these structures into MIS solar cell architectures to quantify PCE enhancement.

Acknowledgements The authors would like to express their sincere gratitude to Muhammad Faisal Ayyaz from the University of Gujrat, Pakistan, for his kind assistance in preparing the graphical abstract. The authors gratefully acknowledge the University of Cagliari, Italy, for its institutional support throughout this research, and the Department of Physics, University of Gujrat, Pakistan, for providing the research facilities and infrastructure that made this work possible. The authors also wish to extend their appreciation to the COMSOL Laboratory team at the University of Gujrat for their invaluable technical guidance and support during the computational aspects of this study.

Authors' Contributions All authors contributed to the study conception and design. MNA developed the simulation methodology, performed the COMSOL Multiphysics simulations, analyzed and interpreted the data, and prepared the original draft of the manuscript. HA, MANG, MR, and RJ contributed to model validation, including mesh convergence analysis, and provided scientific input through manuscript revision, critical review, and discussions. TI and GM supervised the research, provided expert guidance, validated the results, and contributed to the interpretation, discussion, and refinement of the manuscript. All authors reviewed and approved the final version of the manuscript.

Funding Open access funding provided by Università degli Studi di Cagliari within the CRUI-CARE Agreement. The authors declare that there is no funding or grant received during this work.

Data Availability No datasets were generated or analysed during the current study.

Declarations

Competing Interests The authors declare no competing interests.

Open Access This article is licensed under a Creative Commons Attribution 4.0 International License, which permits use, sharing, adaptation, distribution and reproduction in any medium or format, as long as you give appropriate credit to the original author(s) and the source, provide a link to the Creative Commons licence, and indicate if changes were made. The images or other third party material in this article are included in the article's Creative Commons licence, unless indicated otherwise in a credit line to the material. If material is not included in the article's Creative Commons licence and your intended use is not permitted by statutory regulation or exceeds the permitted use, you will need to obtain permission directly from the copyright holder. To view a copy of this licence, visit http://creativecommons.org/licenses/by/4.0/.

References

1. Green MA et al (2024) Solar cell efficiency tables (Version 64). Prog Photovolt Res Appl 32(7):425–441
2. Green MA et al (2025) Solar cell efficiency tables (version 65). Prog Photovoltaics Res Appl 33(1):3–15
3. Massiot I, Cattoni A, Collin S (2020) Progress and prospects for ultrathin solar cells. Nat Energy 5(12)959–972
4. Ramanujam J et al (2016) Inorganic photovoltaics–planar and nanostructured devices. Prog Mater Sci 82:294–404
5. Younsi Z et al (2024) Scrutinizing transport phenomena and recombination mechanisms in thin film Sb2S3 solar cells. Sci Rep 14(1):12460
6. Moustafa M, Abu Waar Z, Yasin S (2025) Optimizing solar performance of CFTSe-based solar cells using MoSe2 as an innovative buffer layers. Sci Rep 15(1):614
7. Zhang L et al (2023) Advances in the application of perovskite materials. Nano-Micro Lett 15(1):177
8. Atwater HA, Polman A (2010) Plasmonics for improved photovoltaic devices. Nat Mater 9(3):205–213
9. Crampton KT, Joly AG, Gong Y, El-Khoury P (2024) Spatiotemporal imaging and manipulation of surface plasmons, Nanophotonics 13(11)1985–1992
10. De Tommasi E et al (2021) Frontiers of light manipulation in natural, metallic, and dielectric nanostructures. La Rivista del Nuovo Cimento 44(1):1–68
11. Hinman SS, McKeating KS, Cheng Q (2017) Surface plasmon resonance: material and interface design for universal accessibility. Anal Chem 90(1):19
12. Qureshi MT et al (2023) Enhanced photocatalytic efficiency and biosensing in plasmonic nanostructures for the detection of bacteria in various analytes. Opt Quant Electron 55(13):1147
13. Li X, Zhu J, Wei B (2016) Hybrid nanostructures of metal/two-dimensional nanomaterials for plasmon-enhanced applications. Chem Soc Rev 45(11):3145–3187
14. Iqbal T et al (2024) Geometrical optimization of TiO2-noble metal grating for enhanced photocatalytic activity and SPR biosensor application, Plasmonics 19(5)2635–2652
15. Brechbuhler R et al (2021) Compact plasmonic distributed-feedback lasers as dark sources of surface plasmon polaritons. ACS Nano 15(6):9935–9944
16. Saeed F, Iqbal T, Al-Zaqri N, Warad I, Sultan MS (2023) Modelling and Optimization of 1D Sinusoidal Plasmonic Grating Application in Solar Cell, Plasmonics 18(3)1117–1127
17. Iqbal M et al (2022) Plasmonic-based Solar Cell: Geometrical Optimization of 1D-nanostructured Grating for Enhanced Efficiency, Plasmonics 17(6)2491–2520
18. Aly AMA, Hussein M, Yahia A, Hameed MFO (2021) Obayya SSA Highly efficient SiO2 trapezoidal grating-based thin-film solar cell. J Opt Soc Am B 38(3):922–931
19. Elewa S, Yousif B, Abo-Elsoud MEA (2021) Improving efficiency of perovskite solar cell using optimized front surface nanospheres grating. Appl Phys A 127(11):854
20. Heidarzadeh H (2019) Incident light management in a thin silicon solar cell using a two-dimensional grating according a Gaussian distribution. Sol Energy 189:457–463
21. Pavithra G, Venkatesha M, Chaya B, Narayan K (2021) Modeling and analysis of grating structure for enhancing the absorbance in organic solar cell, in 2021 2nd International Conference for Emerging Technology (INCET) 1–4:IEEE

22. Rosengart E-H (1977) Pockrand I Influence of higher harmonics of a grating on the intensity profile of the diffraction orders via surface plasmons. Opt Lett 1(6)194–195
23. Ali A, El-Mellouhi F, Mitra A, Aïssa B (2022) Research Progress of Plasmonic Nanostructure-Enhanced Photovoltaic Solar Cells, Nanomaterials 12(5)788
24. Dawood YZ, Salman AH, Al-Hamdani AH, Aljubory AS (2025) Porous silicon formation methods and their photovoltaic applications: a review, WORLD TALENT AND INNOVATION JOURNAL FOR SCIENCE AND ENGINEERING (WTIJSE) 2(2):33–46
25. Jia H, Xie F, Nefzaoui E, Bourouina T, Jiang H, Zhang X (2025) Black silicon nanostructures for solar energy conversion and photonic applications: a review. Adv Photonics 7(3):034004–034004
26. Mula G et al (2026) Dramatic changes induced on porous silicon birefringence by shape-dependent properties. Sci Rep 16(1):15198
27. Rahmouni S, Zighed L (2018) Experimental Study of Porous Silicon Films, in Applications of Silicon Photonics in Sensors and Waveguides: IntechOpen
28. Chao C-TC, Kooh MRR, Lim CM, Thotagamuge R, Mahadi AH, Chau Y-FC (2023) Visible-Range Multiple-Channel Metal-Shell Rod-Shaped Narrowband Plasmonic Metamaterial Absorber for Refractive Index and Temperature Sensing, Micromachines 14(2):340
29. Chou Chau Y-F, Lim CM, Chiang C-Y, Voo NY (2016) i. Muhammad Idris, and, Chai SU Tunable silver-shell dielectric core nanobeads array for thin-film solar cell application. J Nanopart Res 18(4):88
30. Keshavarz Hedayati M, Elbahri M (2016) Antireflective coatings: Conventional stacking layers and ultrathin plasmonic metasurfaces, a mini-review, Materials 9(6):497
31. Martín-Palma RJ, McAtee PD, Ramadan R, Lakhtakia A (2019) Hybrid nanostructured porous silicon-silver layers for wideband optical absorption. Sci Rep 9(1):7291
32. Ramadan R, Manso-Silván M, Martín-Palma RJ (2020) Hybrid porous silicon/silver nanostructures for the development of enhanced photovoltaic devices. J Mater Sci 55(13):5458–5470
33. Lin H et al (2023) Silicon heterojunction solar cells with up to 26.81% efficiency achieved by electrically optimized nanocrystalline-silicon hole contact layers. Nat Energy 8(8):789–799
34. Hossain MK, Shuangyi M, Mukhaimer AW, Rahman MM, Saeed M and, Al RS, Abri (2025) Copper nanoclusters in thin film solar cells: Bridging FDTD analysis and fabrication. J Mater Res Technol, 39, 2518–2526
35. Yu B, Wang Y, Zhang Y, Zhang Z (2023) Self-supporting nanoporous copper film with high porosity and broadband light absorption for efficient solar steam generation. Nano-micro Lett 15(1):94
36. Ahsan S et al (2025) Geometrical optimization of 2D MoS2-Ag rectangular and triangular grating for enhanced solar cell efficiency, *Plasmonics*, vol. 20, no. 1, pp. 325–341
37. Palik ED (1984) Handbook of optical constants (A). J Opt Soc Am A 1:1297
38. Yi X (2025) Plasmon–exciton coupling in two-dimensional materials: fundamentals and applications in nanosensors. Sens Rev pp. 1–25
39. Zhang Y et al (2021) Plasmonic tweezers: for nanoscale optical trapping and beyond. Light: Sci Appl 10(1):59
40. Eslami S, Palomba S (2021) Integrated enhanced Raman scattering: a review. Nano Convergence 8(1):41
41. Iqbal T et al (2023) Efficient plasmonic-based biosensing for mixture of gases-far-and near field analysis. Opt Quant Electron 55(7):647
42. Iqbal T et al (2020) Surface-enhanced Raman scattering (SERS) on 1D nano-gratings, *Plasmonics*, vol. 15, no. 4, pp. 1053–1059
43. Jiang S et al. (2026) Structure-Function Tailoring of Plasmonic Nanomaterials for Thin-Film Photovoltaics. Carbon Energy e70239. https://doi.org/10.1002/cey2.70239
44. Murugan D et al (2024) Recent advances in grating coupled surface plasmon resonance technology. Adv Opt Mater 12(34):2401862
45. Kim H, Yun H, Jeong S, Lee S, Cho E, Rho J (2025) Optical metasurfaces for biomedical imaging and sensing. ACS Nano 19(3):3085–3114
46. Hidayat R, Pradana JS, Fariz A, Komalasari S, Chalimah S, Bahar H (2023) Dual plasmonic modes in the visible light region in rectangular wave-shaped surface relief plasmonic gratings. Sci Rep 13(1):5274
47. Ruiz de Galarreta C et al (2022) Single-step fabrication of high-performance extraordinary transmission plasmonic metasurfaces employing ultrafast lasers. ACS Appl Mater Interfaces 14(2):3446–3454
48. Pan C et al (2024) Large area single crystal gold of single nanometer thickness for nanophotonics. Nat Commun 15(1):2840
49. Sun K et al (2025) Full polarization and high coherence control of thermal emissions via saddle-band dispersion engineering. Nat Commun 16(1):8393
50. Zograf GP, Petrov MI, Makarov SV, Kivshar YS (2021) All-dielectric thermonanophotonics. Adv Opt Photonics 13(3):643–702
51. Polyanskiy MN (2024) Refractiveindex. info database of optical constants. Sci Data 11(1):94
52. Johnson PB, Christy R-W (1972) Optical constants of the noble metals. Phys Rev B 6(12):4370
53. Iqbal T (2013) Nanoplasmonic grating coupler for transducer applications. Queen's University Belfast
54. Qu Y, Liang J, Yan W, Wu Q, Zhu J, Zhou L (2025) Low-loss plasmonics based on alkali metals: from fundamentals to applications: tutorial. Adv Opt Photonics 17(1):1–44
55. SunP, Xu P, Zhu K, Zhou Z (2021) Silicon-based optoelectronics enhanced by hybrid plasmon polaritons: Bridging dielectric photonics and nanoplasmonics. Photonics, vol 8. MDPI, p 482. 11. https://doi.org/10.3390/photonics8110482
56. Poulin M, Skorobogatiy M (2022) Surface Waves on Nonconducting Structured Interfaces. IEEE Trans Antennas Propag 70(11):10691–10705
57. Garcia-Vidal FJ et al (2022) Spoof surface plasmon photonics. Rev Mod Phys 94(2):025004
58. Wang X, Yue H, Liu G, Zhao Z (2011) The application of COMSOL multiphysics in direct current method forward modeling. Procedia Earth Planet Sci 3:266–272
59. Yee K (1966) Numerical solution of initial boundary value problems involving Maxwell's equations in isotropic media. IEEE Trans Antennas Propag 14(3):302–307
60. Gupta K, Meek J (1996) A brief history of the beginning of the finite element method. Int J Numer Methods Eng 39(22):3761–3774
61. Abdelraouf OA, Ahmed A, Eldele E, Omar AA (2025) Physics-informed neural networks in electromagnetic and nanophotonic design, arXiv preprint arXiv:2505.03354,
62. Li S, Zhou L, Panmai M, Xiang J, Lan S (2021) Magnetic plasmons induced in a dielectric-metal heterostructure by optical magnetism, Nanophotonics 10(10)2639–2649
63. Kar C, Jena S, Udupa DV, Rao KD (2023) Tamm plasmon polariton in planar structures: A brief overview and applications. Opt Laser Technol 159:108928
64. Koya AN et al (2021) Nanoporous metals: From plasmonic properties to applications in enhanced spectroscopy and photocatalysis. ACS Nano 15(4):6038–6060
65. Ahmed A, Mehaney A (2019) Ultra-high sensitive 1D porous silicon photonic crystal sensor based on the coupling of Tamm/Fano resonances in the mid-infrared region. Sci Rep 9. https://doi.org/10.1038/s41598-019-43440-y

66. H. Elsayed, M. Medhat, A. Hajjiah, H. Alfassam, M. Abukhadra, and A. Mehaney (2025) "A promising high-sensitive 1D photonic crystal magnetic field sensor based on the coupling of Fano\ Tamm resonance in far IR region," Scientific Reports 15
67. Javaid M, Iqbal T (2016) Plasmonic Bandgap in 1D Metallic Nanostructured Devices, Plasmonics 11(1)167–173
68. Ghaemi HF, Thio T, Grupp DE, Ebbesen TW, Lezec HJ (1998) Surface plasmons enhance optical transmission through subwavelength holes. Phys Rev B 58:6779–6782
69. Raether H (1988) Surface Plasmons on Smooth and Rough Surfaces and on Gratings
70. Vasa P, Lienau C (2017) Strong Light–Matter Interaction in Quantum Emitter/Metal Hybrid Nanostructures. ACS Photonics
71. Guang J et al (2024) Visible light-illuminated gold nanohole arrays with tunable on-chip plasmonic sensing properties. Photonic Sens 14(3):240311
72. Kolwas K, Derkachova A (2020) Impact of the Interband Transitions in Gold and Silver on the Dynamics of Propagating and Localized Surface Plasmons, Nanomaterials 10
73. Pritom YA, Sikder DK, Zaman S, Hossain M (2023) Plasmon-enhanced parabolic nanostructures for broadband absorption in ultra-thin crystalline Si solar cells. Nanoscale Adv 5(18):4986–4995
74. Wang W et al (2017) Broadband optical absorption based on single-sized metal-dielectric-metal plasmonic nanostructures with high-ε ″metals. Appl Phys Lett 110, 10
75. Tang C et al (2024) Ultra-broadband near-infrared absorption enhancement of monolayer graphene by multiple-resonator approach. Diam Relat Mater. https://doi.org/10.1016/j.diamond.2023.110607
76. ElKhamisy K, Abdelhamid H, Elagooz S, El-Rabaie E-S (2022) The efficiency of silicon thin film solar cell: impact of temperature with different surface shapes. Opt Quant Electron 54(1):49
77. Mondal P, Alkhazragi O, Bagci H (2025) Enhanced absorption in thin-film silicon solar cells using a broadband plasmonic nanostructure. Opt Express 33 14:29118–29133.
78. Badri YE et al (2025) Towards Reliable Characterization of Materials'Plasmonic Properties using Fabry-Perot Resonance
79. Erwin W, Zarick H, Talbert E, Bardhan R (2016) Light trapping in mesoporous solar cells with plasmonic nanostructures. Energy Environ Sci 9:1577–1601
80. Wang Y, Liu H, Wang S, Cai M (2022) Hybrid Nanowire–Rectangular Plasmonic Waveguide for Subwavelength Confinement at 1550 Nm, Micromachines, vol. 13
81. Zhao Y, Xu Z (2024) Enhancing and confining light in hybrid plasmonic nanowire-integrated V-groove silicon waveguides. Discover Appl Sci 6:1–12
82. Bian Y, Zheng Z, Zhao X, Zhu J, Zhou T (2009) Symmetric hybrid surface plasmon polariton waveguides for 3D photonic integration. Opt Express 17(23):21320–21325
83. Wei X et al (2024) Plasmonic hybridized modes empowered by strong plasmon interaction in the nanograting-dielectric-metal stacked structure. J Phys D 57
84. Din R, Ali H (2024) Ahmad R Manipulation of surface plasmon-polaritons in nanocomposite-metal-nanocomposite waveguide. Phys Lett A
85. Bian Y et al (2013) Highly Confined Hybrid Plasmonic Modes Guided by Nanowire-Embedded-Metal Grooves for Low-Loss Propagation at 1550 nm. IEEE J Sel Top Quantum Electron 19:4800106–4800106
86. Chau C et al (2021) Significantly enhanced coupling effect and gap plasmon resonance in a MIM-cavity based sensing structure. Sci Rep, 11
87. Bermel P, Luo C, Zeng L, Kimerling L, Joannopoulos J (2007) Improving thin-film crystalline silicon solar cell efficiencies with photonic crystals. Opt Express 15(25):16986–17000
88. Schatz G, The Optical Properties of Metal Nanoparticles et al (2003) The Influence of Size, Shape, and Dielectric Environment. J Phys Chem B 107:668–677
89. Bekshaev A, Angelsky O, Zheng J, Hanson S, Zenkova C (2021) Microscopic analysis of the energy, momentum, and spin distributions in a surface plasmon-polariton wave. Opt Mater Express
90. Maier S, Atwater H, Plasmonics (2005) Localization and guiding of electromagnetic energy in metal/dielectric structures. J Appl Phys 98:11101
91. Sørensen L et al (2021) Plasmonic Enhancement of Local Fields in Ultrafine Metal Nanoparticles. J Phys Chem C
92. Ayache L, Nourani KM, Azizi S (2024) A surface plasmon resonance biosensor for bacteria and virus detection: A Comsol Multiphysics simulation. Synthesis Sinter
93. Yang X et al (2023) Hot Spot Engineering in Hierarchical Plasmonic Nanostructures, Small
94. Wy Y, Jung H, Hong J, Han S (2022) Exploiting Plasmonic Hot Spots in Au-Based Nanostructures for Sensing and Photocatalysis. Acc Chem Res
95. Borah R, Verbruggen S (2020) Silver–Gold Bimetallic Alloy versus Core–Shell Nanoparticles: Implications for Plasmonic Enhancement and Photothermal Applications. J Phys Chem C
96. Arnold M, Blaber M (2009) Optical performance and metallic absorption in nanoplasmonic systems. Opt Express 17(5):3835–3847
97. Rodriguez R et al (2018) Aluminum and copper nanostructures for surface-enhanced Raman spectroscopy: A one-to-one comparison to silver and gold. Sens Actuators B
98. Boroviks S et al (2021) Extremely confined gap plasmon modes: when nonlocality matters. Nat Commun 13. https://doi.org/10.1038/s41467-022-30737-2
99. Borah R, Ninakanti R, Bals S, Verbruggen SW (2022) Plasmon resonance of gold and silver nanoparticle arrays in the Kretschmann (attenuated total reflectance) vs. direct incidence configuration. Sci Rep 12(1):15738
100. Rezaeian A, Hosseini Farzad M (2024) Magneto-optical heterostructures with second resonance of transverse magneto-optical Kerr effect. Sci Rep 14(1):3493
101. Wang Q et al (2024) Research on fiber optic surface plasmon resonance biosensors: A review. Photonic Sens 14(2):240201
102. Darmanyan SA, Zayats AV (2003) Light tunneling via resonant surface plasmon polariton states and the enhanced transmission of periodically nanostructured metal films: An analytical study. Phys Rev B 67(3):035424
103. Raether H (2006) Surface plasmons on smooth surfaces. Surface plasmons on smooth and rough surfaces and on gratings. Springer, pp 4–39
104. Zakharian AR, Moloney JV, Mansuripur M (2007) Surface plasmon polaritons on metallic surfaces. Opt Express 15(1):183–197
105. Celebrano M et al (2010) Efficient coupling of single photons to single plasmons. Opt Express 18(13):13829–13835
106. Makarenko K et al (2020) Efficient Surface Plasmon Polariton Excitation and Control over Outcoupling Mechanisms in Metal–Insulator–Metal Tunneling Junctions. Adv Sci, 7
107. Erwin WR, Zarick HF, Talbert EM, Bardhan R (2016) Light trapping in mesoporous solar cells with plasmonic nanostructures. Energy Environ Sci 9(5):1577–1601
108. Fei Guo C, Sun T, Cao F, Liu Q, Ren Z (2014) Metallic nanostructures for light trapping in energy-harvesting devices. Light: Sci Appl 3(4):e161–e161
109. Wu R et al (2021) Localized Plasmon Field Effect of Gold Clusters Embedded in Nanoporous Silicon. Adv Opt Mater, 9

110. Amran T, Hashim M, Al-Obaidi N, Yazid H, Adnan R (2013) Optical absorption and photoluminescence studies of gold nanoparticles deposited on porous silicon. Nanoscale Res Lett 8:35–35
111. Agafilushkina S et al (2020) Raman Signal Enhancement Tunable by Gold-Covered Porous Silicon Films with Different Morphology. Sensors, 20
112. Biteen J, Pacifici D, Lewis N, Atwater H (2005) Enhanced radiative emission rate and quantum efficiency in coupled silicon nanocrystal-nanostructured gold emitters. Nano Lett 5(9):1768–1773
113. Trinh HT, Dang H, Van Nguyen D, Chu HM (2024) Low ohmic loss hybrid gap plasmonic waveguide with miniaturized metal-dielectric interface. Jpn J Appl Phys, 63
114. Huang C-C, Chang R-J, Huang CC (2021) Nanostructured hybrid plasmonic waveguide in a slot structure for high-performance light transmission. Opt Express 29(18):29341–29356
115. Delacour C et al (2010) Efficient directional coupling between silicon and copper plasmonic nanoslot waveguides: toward metal-oxide-silicon nanophotonics. Nano Lett 10(8)2922–2926
116. Fedyanin D, Yakubovsky D, Kirtaev R, Volkov V (2016) Ultralow-Loss CMOS Copper Plasmonic Waveguides, Nano letters 16(1):362–366

Publisher's Note Springer Nature remains neutral with regard to jurisdictional claims in published maps and institutional affiliations.